RSC Advances

PAPER

View Article Online
View Journal | View Issue



Cite this: *RSC Adv.*, 2025, **15**, 31788

# Enhancing the multifunctional properties of polycaprolactone/chitosan films with zirconium dioxide nanoparticles for biomedical and flexible optoelectronic applications

Qasim Shakir Kahdim,[a] Zohra Benzarti, *[bc] Mohanad H. Mousa,[d] Maher Hassan Rasheed,[e] Najmeddine Abdelmoula[b] and Ali Khalfallah[cf]

This study addresses the growing need for sustainable and multifunctional materials by developing novel polycaprolactone (PCL)/chitosan (CS)/zirconium dioxide ($ZrO_2$) nanocomposite films. While PCL and CS offer biocompatibility and biodegradability, their combined use presents limitations for advanced applications requiring specific functional features. The incorporation of $ZrO_2$ nanoparticles aims to overcome these limitations and create materials with enhanced mechanical, electrical, optical, and antibacterial properties. The nanocomposites were synthesized *via* a simple casting method, and their properties were comprehensively characterized. Results show that the addition of $ZrO_2$ significantly improves the mechanical, electrical, optical, and antibacterial characteristics of the PCL-CS copolymer. Specifically, a 2 wt% $ZrO_2$ concentration yielded an optimal balance of mechanical strength, stiffness, ductility, and toughness, with a 63% increase in ultimate tensile strength and a 93% increase in toughness compared to neat PCL-CS. The electrical conductivity was significantly enhanced with increasing $ZrO_2$ content and temperature, and the dielectric properties were improved, positioning $ZrO_2$ as a mid-range dielectric filler. Optical analysis revealed that $ZrO_2$ content tunes the absorbance, energy gap, and refractive index, making these films suitable for optical applications. Furthermore, the nanocomposites exhibited remarkable antibacterial activity against both Gram-positive *Staphylococcus aureus* and Gram-negative *Escherichia coli*, with inhibition zones increasing with $ZrO_2$ concentration, demonstrating the synergistic effect between chitosan and $ZrO_2$. These findings highlight the potential of PCL-CS/$ZrO_2$ nanocomposite films as versatile and sustainable alternatives for a wide range of applications, including biomedical devices, flexible optoelectronics, and smart packaging.

Received 22nd July 2025
Accepted 25th August 2025

DOI: 10.1039/d5ra05303j

rsc.li/rsc-advances



## 1. Introduction

Rising global concerns over plastic waste from synthetic polymers have driven researchers and industries to explore sustainable alternatives. Biopolymers have garnered significant attention due to their eco-friendly properties and potential to mitigate environmental pollution.[1] These materials are widely utilized in agriculture, textiles, and biomedical applications, such as drug delivery systems and tissue engineering scaffolds.[2,3] Among biopolymers, polycaprolactone (PCL), an aliphatic semi-crystalline polyester, stands out for its biocompatibility, appropriate mechanical properties, and approval by the U.S. Food and Drug Administration (FDA).[4,5] Consequently, PCL is extensively employed in biomedical applications, including tissue engineering scaffolds and controlled drug delivery systems.[6] However, its hydrophobicity limits interactions with biological tissues, restricting broader applications.[7] To overcome this limitation, strategies such as copolymerization[8] or polymer blending[9] have been explored. Blending PCL with hydrophilic polymers, such as poly(ethylene oxide), enhances water permeability and hydrolytic degradation but often reduces tensile strength due to decreased matrix crystallinity.[7] Polymer blending represents an effective technique for adjusting polymer hydrophilicity while maintaining mechanical integrity. Indeed, blending with chitosan (CS), a biodegradable polysaccharide derived from the *N*-deacetylation of

[a]*Department of Science, College of Basic Education, University of Babylon, Babylon, Iraq*

[b]*Laboratory of Multifunctional Materials and Applications (LaMMA), Faculty of Sciences of Sfax, University of Sfax, BP 1171, 3000 Sfax, Tunisia. E-mail: zohra.benzarti@fss.usf.tn*

[c]*University of Coimbra, CEMMPRE, ARISE, Department of Mechanical Engineering, Rua Luís Reis Santos, Coimbra, 3030-788, Portugal*

[d]*Shatrah Technical Institute, Southern Technology University (STU), Basra, Iraq*

[e]*Department of Science, College of Basic Education, University of Babylon, Babylon, Iraq*

[f]*DGM, Institut Supérieur des Sciences Appliquées et de Technologie de Sousse, Université de Sousse, Cité Ibn Khaldoun, 4003 Sousse, Tunisia*

chitin (sourced from shrimp and crab processing waste), offers a promising alternative.[10] Chitosan is FDA-approved and biocompatible, and exhibits antimicrobial properties, making it ideal for wound dressings and skin tissue regeneration.[11] Blending PCL with CS provides multiple benefits: (i) both polymers are biocompatible, suitable for drug delivery and wound healing;[12] (ii) CS degrades enzymatically, complementing PCL's hydrolytic degradation mechanisms; (iii) PCL exhibits low tensile strength which is further enhanced by blending with CS, improving stiffness and structural integrity for load-bearing applications;[13] (iv) CS's hydrophilicity improves PCL's wettability and cell adhesion;[14,15] and (v) CS reduces the composite cost as a cost-effective biopolymer when blended with PCL.[16] Studies also show that PCL-CS composites exhibit enhanced mechanical properties over neat PCL, with tensile strength increasing by 15–30% and Young's modulus improving at optimal CS concentrations (5–10%).[17] However, these blends face limitations in applications requiring electrical functionality, such as implantable medical devices and wearable health monitors, which require biocompatibility, biodegradability, suitable mechanical properties and electrical functionality. The dielectric properties of the composite can be enhanced by blending CS with PCL, as this reduces crystallinity and promotes an amorphous structure, thereby improving ionic mobility and dielectric uniformity.[18,19] While blending CS with PCL improves dielectric properties by reducing crystallinity and enhancing ionic mobility,[20] both polymers exhibit low dielectric constants, and at higher frequencies, dielectric losses can become substantial, limiting their performance in high-permittivity applications.[21] In terms of interfacial compatibility, the $-NH_2$ and –OH groups in chitosan facilitate bonding with PCL, minimizing phase separation and enhancing dielectric uniformity, which reduces defects that may lead to leakage currents.[22] To remediate the low mechanical properties of PCL or PCL-CS for specific biomedical applications which demand high-performance materials and to address challenges related to structural integrity, incorporating fillers into PCL-CS composites has been explored. Fillers such as hydroxyapatite, nanofibrillated chitosan, and metal oxide nanoparticles (*e.g.*, $TiO_2$, $CeO_2$) mitigate phase separation and enhance mechanical properties, hydroxyapatite increases compressive strength by up to 45% for bone applications, while metal oxides reinforce without sacrificing elasticity.[23] However, limitations persist, including filler agglomeration, non-uniform dispersion, phase compatibility issues, long-term biocompatibility concerns, accelerated degradation rates, and scalability challenges for industrial production.[24] Among available nanoparticles, zirconium dioxide ($ZrO_2$) is well-known for its favorable dielectric properties in electronic manufacturing.[25] $ZrO_2$ has a high dielectric constant of up to 33, significantly boosting the permittivity of the polymer matrix, which is essential for energy storage applications, such as gate dielectrics in transistors, enabling greater charge storage under an electric field.[26,27] Additionally, $ZrO_2$'s wide bandgap (5–7 eV) reduces leakage current under high electric field conditions.[25] Furthermore, its high thermal stability and resistance to phase transitions up to 1200 °C make it ideal for dielectric applications in harsh environments.[25] The addition of $ZrO_2$ creates a heterogeneous interphase within the polymer matrix, promoting interfacial polarization. This results in charge trapping at the interface, reducing recombination losses and enhancing charge storage.[28] Similar effects have been observed in $ZrO_2$/CS composites, where charge separation enhances catalytic efficiency.[29] In dielectric environments, this also increases breakdown strength and energy storage capacity.[28,29] Previous studies have reported that incorporating $ZrO_2$ nanoparticles enhances biocompatibility and bioactivity. Catauro *et al.*[30] found that $ZrO_2$ in PCL hybrid coatings improves bioactivity by promoting apatite layer formation on the surface when soaked in simulated body fluid, with calcium phosphate deposition increasing with higher PCL content. Similarly, Shanmugam *et al.*[31] reported that 1 wt% $ZrO_2$ exhibited enhanced suitability for tissue engineering applications, attributed to improve *in vitro* biocompatibility, protein absorption, and antibacterial efficacy against *Staphylococcus aureus* and *Escherichia coli*.

In this study, we blend PCL-CS copolymer, with $ZrO_2$ to develop a novel nanocomposite films. While prior studies on PCL/$ZrO_2$ or CS/$ZrO_2$ composites have demonstrated improvements in specific properties, no comprehensive research has explored the synergistic effects of PCL, CS and $ZrO_2$ combination. This work stands out by integrating these three components to synthesize nanocomposite films with enhanced electrical, optical, mechanical, and biological properties. Unlike prior studies, we focus on the influence of $ZrO_2$ concentration on the PCL-CS copolymer, aiming to achieve unique characteristics and increased multifunctionality for biomedical applications, flexible optoelectronics, and smart packaging. By evaluating the electrical, optical, mechanical and antibacterial properties of PCL-CS/$ZrO_2$ nanocomposite films, we demonstrate that the optimal composition outperforms conventional composites (*e.g.*, PCL-CS, PCL/$ZrO_2$ or CS/$ZrO_2$), offering a sustainable and versatile alternative to existing materials.

## 2. Materials and methods

Chitosan (CS) with low molecular weight and >75% degree of deacetylation was purchased from Central Drug House (P) Ltd, New Delhi, India. Polycaprolactone (PCL) with an average $M_n$ of 80 000 was supplied by Reagent World.com (**https://www.world.com**), Ontario, USA. Zirconium oxide nanoparticles ($ZrO_2$, CAS No. 1314-23-4) with a minimum assay of 99.0% (trace metal analysis), with an average diameter of 100 nm, were procured from HiMedia Laboratories Pvt. Ltd. Acetic acid and all other chemical reagents were sourced from laboratories of the College of Basic Education, University of Babylon.

### 2.1. Synthesis of PCL-CS/$ZrO_2$ nanocomposites

PCL-CS/$ZrO_2$ nanocomposites were prepared by a simple casting method. Initially, PCL (0.6 g) was dissolved in a glacial acetic acid : formic acid solution (1 : 3 by volume ratio) under magnetic stirring at room temperature for 1.5 h to ensure complete dissolution of the PCL. Subsequently, CS solution (0.4 g of CS

dissolved in a glacial acetic acid : formic acid solution (1 : 3 by volume ratio)) was added to the PCL solution. The entire mixture (60 wt% PCL and 40 wt% CS) was stirred for 3 hours at room temperature to obtain a homogeneous mixture. Similarly, zirconium oxide ($ZrO_2$) nanoparticles were weighed and then mixed with deionized water, and the suspension was dispersed in an ultrasonic bath at an oscillation frequency of 50 kHz at 80 °C for 10 min. Aqueous $ZrO_2$ suspension was gradually added dropwise to the PCL-CS solution to get PCL-CS/$ZrO_2$ nanocomposites with different $ZrO_2$ concentrations (2 wt%, 4 wt%, and 6 wt%). Finally, 20 mL of the mixed solution was poured onto a glass Petri dish and then dried in a recirculating air oven at 40 °C for one week. The previously prepared PCL-CS/$ZrO_2$ nanocomposites were peeled and stored in a desiccator before any assay.

### 2.2. Material characterization

X-ray diffraction (XRD) measurements were conducted on a Rigaku Smartlab diffractometer (Tokyo, Japan) using Cu Kα radiation ($\lambda$ = 1.54060 Å) at 40 kV and 50 mA. The setup employed a Bragg–Brentano configuration with a step size of 0.02°. Fourier transform infrared spectroscopy (FTIR) spectra of the PCL-CS/$ZrO_2$ nanocomposites were acquired using a Thermo Nicolet Nexus 670 spectrophotometer (USA) in the range of 500–4000 $cm^{-1}$ at room temperature.

The surface features of the PCL-CS/$ZrO_2$ nanocomposites were investigated using a Hitachi SU3800 scanning electron microscope (Tokyo, Japan) in secondary electron mode. The chemical composition, including zirconium, was determined through energy-dispersive X-ray spectroscopy (EDS) with a Bruker Nano System (Berlin, Germany) configured at a 30 keV accelerating voltage.

Mechanical testing was carried out using a tensile testing machine (Shimadzu AGS-X, 1 kN) installed in the Department of Mechanical Engineering at the University of Coimbra. Samples were cut from PCL-CS/$ZrO_2$ films to match the dimensions of the gauge section used in uniaxial tensile testing (length/width ratio ≥4). They were loaded at a stroke rate of 0.5 mm $min^{-1}$ until fracture. The derived results are the force-displacement curves used to characterize the mechanical properties of the samples. At least three tests were performed for each composition to determine the average tensile curve and to estimate the resulting measurement errors.

Electrical measurements were conducted using a DC Keithley 2450 Digital Multimeter (DMM) and Source Measure Unit (SMU). The read pulse duration was fixed at 200 μs, and the interpulse time between read and write operations was set to 700 μs. The DC electrical conductivity of the nanocomposites can be calculated as follows:[32]

$$\sigma_{DC} = \frac{1}{\rho_V} = \frac{t}{R_V A_s} \quad (1)$$

where, $\rho_{DC}$ represents the electrical resistivity, $t$ denotes the thickness, $R_V$ is the bulk electrical resistance, and $A_s$ defines the area of the sample.

Nanocomposite film thickness was determined using a Lambda Limf-10 instrument. This method relies on analysing the interference patterns generated by light reflected from the film's surface and the substrate interface. Employing a 632 nm He–Ne laser, the thickness was calculated from the difference in optical path lengths between these reflections. The nanocomposite film thicknesses ranged from 75 μm to 81 μm.

Thermal activation energy of nanocomposites was calculated using the following equation:[33]

$$\sigma_{DC} = \sigma_0 \exp\left(-\frac{E_a}{k_\beta T}\right) \quad (2)$$

where, $\sigma_0$ denotes the pre-exponential factor, $E_a$ defines the activation energy and $k_\beta$ represents the Boltzmann constant.

The dielectric constant ($\varepsilon'$) of the nanocomposites was determined using this relation:[34]

$$\varepsilon' = \frac{C_p}{C_0} \quad (3)$$

where, $C_p$ is the parallel capacitance and $C_0$ defines the vacuum capacitance.

The dielectric loss ($\varepsilon''$) of the nanocomposites was calculated as follows:[35]

$$\varepsilon'' = \varepsilon' D \quad (4)$$

where, $D$ is the dispersion factor.

The HIOKI 3532-50 LCR HiTESTER AC integrated circuit, governed by an ATmega128 microprocessor, was utilized to determine device resistance, capacitance, inductance, dissipation factor, and quality factor. The AC electrical conductivity of the nanocomposites is calculated using the following equation:[35]

$$\sigma_{AC} = \omega \varepsilon_0 \varepsilon'' \quad (5)$$

where $\omega$ is the angular frequency and $\varepsilon_0$ represents the vacuum permittivity ($8.8542 \times 10^{-12}$ F $m^{-1}$). The operating frequency ranges from 100 Hz to 5 MHz.

The UV-visible spectrophotometer (Shimadzu, UV-1800A) was used to obtain transmission and then absorbance curves within the 200–1000 nm spectral range at room temperature. The nanocomposite films were directly placed in the UV-visible spectrophotometer for analysis and were not supported on any external substrate during the UV-vis absorbance measurements.

The absorption coefficient ($\alpha$) of nanocomposites was determined as a function of the photon energy of the incident light using the following relation:[36]

$$\alpha = 2.303\left(\frac{A}{t}\right) \quad (6)$$

where, $A$ represents the absorbance and $t$ defines the thickness of the sample.

The values of the optical energy gap ($E_g$) of the nanocomposites were determined using the following equation:[34]

$$(\alpha h\nu)^m = B(h\nu - E_g) \quad (7)$$

where, $h\nu$ denotes the photon energy, $B$ is a constant, and $m = 3$ or 2 (forbidden or allowed indirect transitions).

The refractive index ($n$) and the extinction coefficient ($k$) are determined using these equations:[34]

$$n = \frac{1+\sqrt{R}}{1-\sqrt{R}} \quad (8)$$

$$k = \frac{\alpha\lambda}{4\pi} \quad (9)$$

where, $R$ represents the reflectance and $\lambda$ defines the photon wavelength.

The real ($\varepsilon_r$) and imaginary ($\varepsilon_i$) parts of dielectric constant were calculated using the following equations:[34]

$$\varepsilon_r = n^2 - k^2 \quad (10)$$

$$\varepsilon_i = 2nk \quad (11)$$

Antibacterial activities of PCL-CS/$ZrO_2$ nanocomposites were evaluated using the Kirby–Bauer disk diffusion method.[37,38] Sterile inoculation loops were employed to collect four colonies of Gram-positive bacterium *Staphylococcus aureus* (ATCC 29213) and Gram-negative bacterium *Escherichia coli* (ATCC 35218). The nanocomposite-containing plates were incubated at 37 °C for 24 hours before being analysed. Following incubation, the presence of inhibition zones (clear halos indicating bacterial growth suppression) was observed. The diameter of the resulting inhibition zones was measured to quantify the antibacterial effect. Antibacterial assays for nanocomposites were carried out in duplicate.

# 3. Results and discussion

## 3.1. Structural study

Fig. 1 presents XRD patterns of neat PCL-CS copolymer, and the PCL-CS/$ZrO_2$ samples by varying $ZrO_2$ contents from 2% to 6%. For neat PCL-CS composition (*i.e.*, 0 wt% $ZrO_2$), a wide diffraction peak centered around 20° is observed, indicating a semicrystalline structure. The detected peak suggests a strong interaction between the CS and PCL polymers, showing inherent compatibility and miscibility.[39] Distinctive XRD peaks for CS are observed at 19.3°, 20.0°, and 26.3° corresponding to crystalline reflections of (110), (120), and (101), respectively.[40] Relevant characteristic XRD peaks of PCL are obtained at 21°, 22° and 24°, corresponding to the (110), (111), and (200) planes.[41] The presence of $ZrO_2$ nanoparticles led to the emergence of additional peaks. In all three samples containing $ZrO_2$, the crystalline phase of $ZrO_2$ is identified as evidenced by sharp peaks. The preferential peaks of their crystalline structure are assigned to monoclinic (M) and tetragonal (T) crystalline systems, in accordance with JCPDS card numbers 81-1314 and 81-1544, respectively.[42] Using Debye–Scherrer formula,[43] the determined crystallite size of $ZrO_2$ was found to vary between 21 and 24 nm.

It is worth noting that 6% of $ZrO_2$ content shows a reduction in the intensity of the diffraction peaks, suggesting strong interaction between $ZrO_2$ nanoparticles and polymers. Such interactions may lead to a tradeoffs structural stability within the PCL-CS blend.[44]

## 3.2. Vibrational study

Fig. 2 shows the FTIR spectra of the pure PCL-CS and PCL-CS/$ZrO_2$ nanocomposites. Peaks characteristic of PCL are found at 725, 1284, 1471, and 1732 $cm^{-1}$ representing C–O stretching, C–O–C stretching, $CH_2$ symmetric stretching, and C=O bonds, respectively.[45,46] Likewise, the prominent peaks of CS, observed at 890, 1074, 1165, 1630 $cm^{-1}$, 2815 $cm^{-1}$, and 3445 $cm^{-1}$, are assigned to the $CH_3OH$ stretching, C–O bonds, C–O–C bridge asymmetric stretching, N–H bending, C–H stretching, and hydrogen bonded O–H stretching, respectively.[40,45,46]

The FTIR spectra of the nanocomposites largely retain the characteristic peaks of PCL-CS, with slight shifts observed due to hydrogen bonding and dipole–dipole interactions between PCL and CS. Upon $ZrO_2$ nanoparticle incorporation,

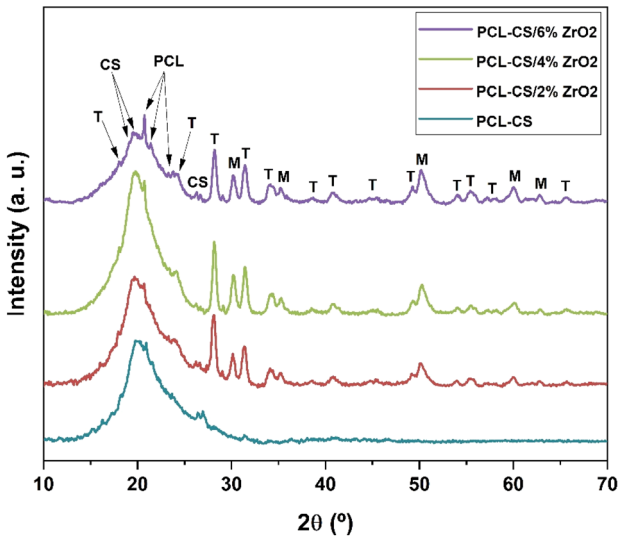


Fig. 1 XRD patterns of PCL-CS/$ZrO_2$ nanocomposite films with different $ZrO_2$ concentrations (0%, 2%, 4%, and 6%).

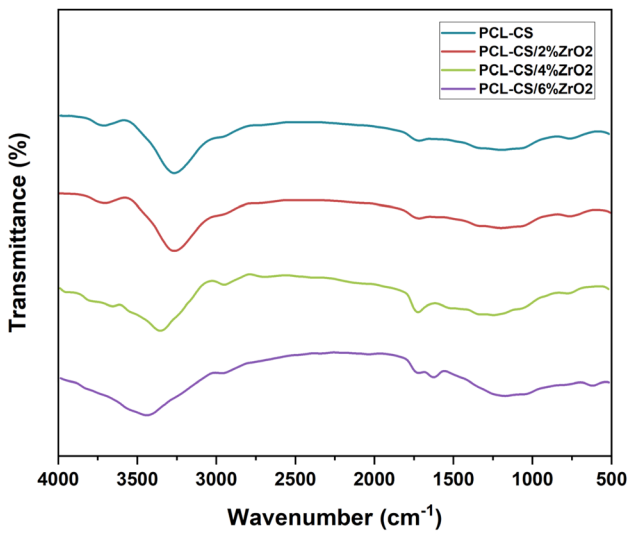


Fig. 2 FTIR spectra of PCL-CS/$ZrO_2$ nanocomposite films.

a noticeable shift in the broad 3500 $cm^{-1}$ peak in PCL-CS/$ZrO_2$ nanocomposites indicates interactions between $ZrO_2$ surface hydroxyl groups and chitosan's functional groups, forming new hydrogen bonds. Additionally, $Zr^{4+}$ centers may coordinate with oxygen atoms in PCL carbonyl groups, further altering the local chemical environment. These interactions disrupt the original PCL-CS hydrogen bonding network, establishing new interfacial bonds with $ZrO_2$ involving Zr–OH groups and confirming strong polymer–nanoparticle interactions.[12] Such modifications are expected to enhance interfacial adhesion and overall structural integrity. This shift becomes more pronounced with increasing $ZrO_2$ content. Notably, at a 6 wt% $ZrO_2$ content, new peaks are observed around 1550 $cm^{-1}$, corresponding to the –OH group, and 560 $cm^{-1}$, associated to the Zr–O stretching vibrations, confirming the successful incorporation of $ZrO_2$ nanoparticles.[47,48]

### 3.3. Morphological study

Fig. 3 shows the morphological structure and elemental composition of the PCL-CS/$ZrO_2$ nanocomposites using SEM and EDS chemical analyses. Fig. 3a depicts the surface of (PCL-CS), where it appears dense and homogeneous, with microporosity within the structure. The porosity is an essential aspect in the healing process, facilitating nutrient transport and vascularization.[49,50]

Fig. 3b and c show the surface of the PCL-CS/$ZrO_2$ nanocomposite with $ZrO_2$ content of 2 wt% and 4 wt%, respectively. They revealed the uniform dispersion of globular $ZrO_2$ nanoparticles within the PCL-CS matrix. This phenomenon is attributed to electrostatic attraction between the cationic component of the PCL-CS matrix and the surface-charged of $ZrO_2$ nanoparticles. Conversely, the SEM image (Fig. 3d) for the 6 wt% $ZrO_2$ nanocomposite reveals a highly clustered microstructure, with numerous agglomerates of $ZrO_2$ nanoparticles forming irregular, dense clusters across the copolymer matrix. It shows a rough, uneven surface with varying particle sizes, suggesting poor dispersion at this concentration. The observed agglomeration at this 6 wt% $ZrO_2$ concentration suggests a potential influence on the overall performance. These agglomerates can appear significantly larger than the primary nanoparticle size due to the tendency of nanoparticles to self-assemble or clump together, especially when their surface energy is high or dispersion is challenging.[51] It was reported that the aggregated nanoparticles act as stress concentration points, reducing elongation and toughness, while increasing tensile strength and stiffness.[52,53] The EDS analysis discloses that the PCL-CS copolymer comprises carbon, nitrogen, and oxygen atoms (PCL-CS), and $ZrO_2$. The detection of these elements confirms the successful formation of the nanocomposite materials.

### 3.4. Mechanical properties

Tensile tests were carried out on PCL-CS/$ZrO_2$ nanocomposite films. The obtained raw force-displacement data were converted

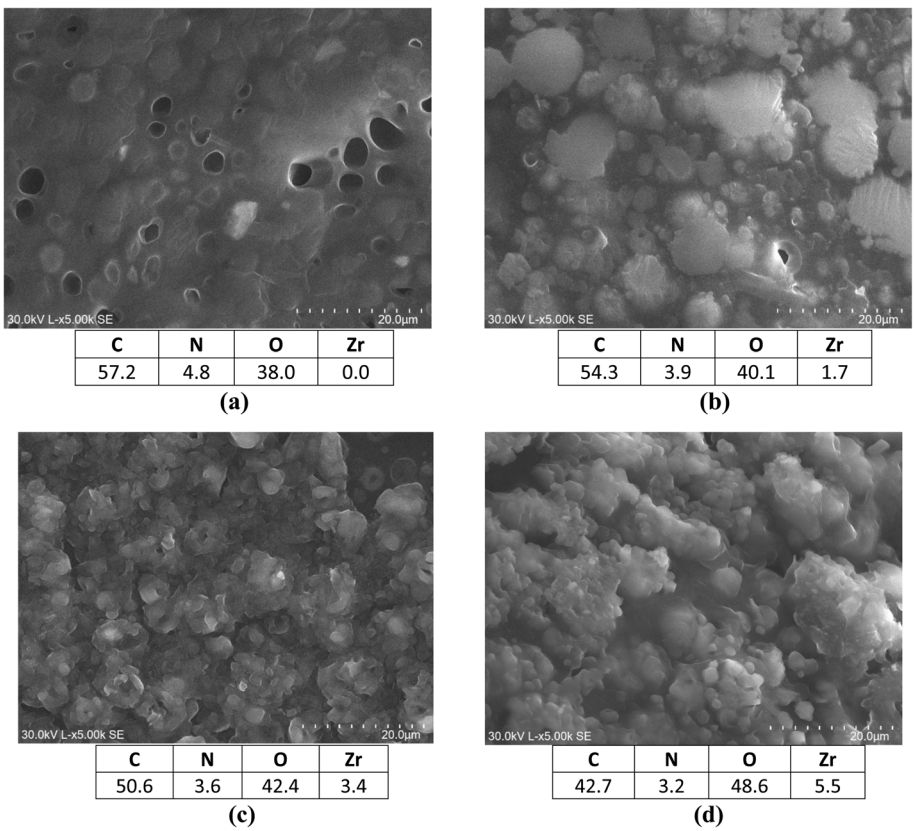


Fig. 3 SEM micrographs and EDS chemical analysis of PCL-CS/$ZrO_2$ nanocomposite films: (a) 0 wt%, (b) 2 wt%, (c) 4 wt%, and (d) 6 wt%.

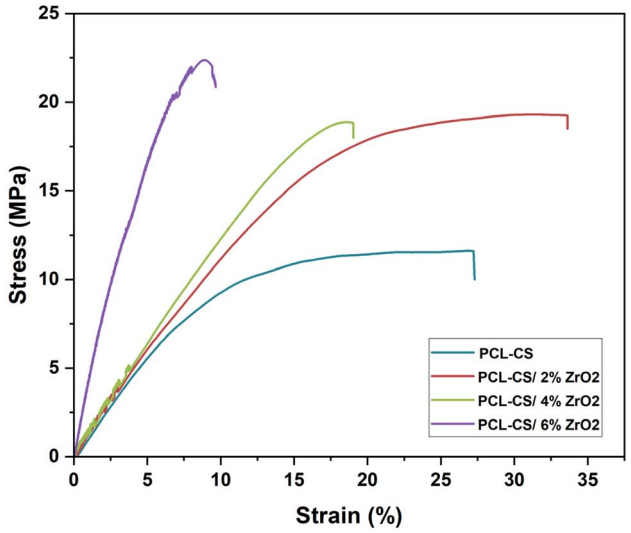


Fig. 4 Stress–strain curves obtained for different PCL-CS/$ZrO_2$ nanocomposite films.

into stress–strain curves by normalizing force and displacement to the sample's initial cross-sectional area and gauge length. Increasing $ZrO_2$ content discloses a clear enhancement of mechanical properties in terms of strength, as shown in Fig. 4, with key results listed in Table 1.

The 0 wt% PCL-CS/$ZrO_2$ sample (neat PCL-CS) exhibits the lowest stiffness and ultimate tensile strength (UTS), with a Young's modulus ($E$) of 116 MPa, an UTS, reaching 11.6 MPa at a strain to failure $\varepsilon_f$ of 27.4%. These findings are compared to reported values in the literature.[54] Adding 2 wt% $ZrO_2$ significantly improves UTS, achieving 18.9 MPa (an increase of 63% compared to neat PCL-CS), and slightly increasing the stiffness compared to the neat PCL-CS sample. This composition achieves the highest toughness ($U_T$: ability to absorb energy and plastically deform before fracture), reaching 466.9 $\times$ $10^3$ J $m^{-3}$ (an increase of ~93% compared to neat PCL-CS copolymer), while achieving a higher strain to failure $\varepsilon_f$ of 33.6% and an increase of the modulus of resilience ($Y_{0.2\%}{}^2/2E$: which measures elastic energy storage capacity) of 12%, indicating optimal balance between strength and energy absorption capacity.

The 4 wt% $ZrO_2$ sample slightly increases stiffness, as indicated by its Young's modulus of 133 MPa, with UTS of 19.4 MPa, close to that obtained for the 2 wt% $ZrO_2$ sample (18.9 MPa). However, this occurs at a reduced strain of 44% compared to the 2 wt% composite, suggesting decreased ductility.

The 6 wt% $ZrO_2$ composite demonstrates the highest Young's modulus ($E$ = 393 MPa), yield stress ($Y_{0.2\%}$ = 9.6 MPa) and (UTS = 22.4 MPa). However, this increase in strength is accompanied by a significant reduction in ductility, with fracture occurring at a strain at failure $\varepsilon_f$ of just 9.7%, reflecting significant embrittlement. The modulus of resilience increases with reinforcement, peaks at 0.117 MPa for the 6 wt% $ZrO_2$ composite, but this is associated with the lowest toughness ($U_T$ = 141.2 $\times$ $10^3$ J $m^{-3}$), reflecting a limited elastic region preceding fracture.

In summary, these findings suggest that 2 wt% $ZrO_2$ provides the best balance of strength, stiffness, ductility and toughness, making it suitable for biomedical devices requiring robustness and flexibility. Enhanced UTS and $Y_{0.2\%}$ up to 4 wt% $ZrO_2$ reflects efficient load transfer from the polymer matrix to well-dispersed $ZrO_2$ nanoparticles, as observed in SEM images (Fig. 3b). However, at 6 wt%, nanoparticle agglomeration (Fig. 3d) forms stress concentration sites, causing premature fracture. For comparison, solvent-cast PCL-CS films with 2 wt% $TiO_2$ exhibited a 35% UTS increase relative to unfilled composites.[55]

The observed enhancement in mechanical properties of PCL-CS/$ZrO_2$ composites with filler concentration, as evidenced by Fig. 4 and Table 1, is attributable to interfacial interactions, stress distribution, and microstructural changes. The mechanical behavior of (PCL-CS/$ZrO_2$) composites is governed by complex interfacial interactions and filler dispersion dynamics. Chitosan acts as a coupling agent, enhancing interfacial shear strength (IFSS) between PCL and $ZrO_2$ attributed to hydrogen bonding and polar interactions between chitosan's hydroxyl/amine groups and $ZrO_2$ surface sites.[56] Despite the presence of surface hydroxyl groups on $ZrO_2$, as evidenced by the broadening and shift of the peak 3500 $cm^{-1}$ in the FTIR spectrum (Fig. 2), which can attract moisture and potentially reduce mechanical performance, the observed increase in mechanical properties with higher $ZrO_2$ content can be attributed to several reinforcing mechanisms that outweigh this drawback. Firstly, $ZrO_2$ nanoparticles possess a high elastic modulus and hardness, providing significant reinforcement to the polymer matrix. Secondly, the surface hydroxyl groups, while hydrophilic, facilitate strong interfacial interactions through hydrogen bonding with chitosan's hydroxyl and amino groups and coordination with the carbonyl groups of PCL. These interactions enhance stress transfer efficiency between the polymer chains and the rigid ceramic phase.[57] Additionally, $ZrO_2$ nanoparticles act as physical crosslinking points, restricting polymer chain mobility and improving stiffness and

Table 1 Mechanical properties of PLC-CS nanocomposites as a function of $ZrO_2$ content, derived from tensile testing

| Sample | Young's modulus $E$ (MPa) | Yield stress $Y_{0.2\%}$ (MPa) | Ultimate tensile strength UTS (MPa) | Strain at failure $\varepsilon_f$ (%) | Toughness $U_T$ ($\times 10^3$ J $m^{-3}$) | Modulus of resilience $Y_{0.2\%}{}^2/2E$ (MPa) |
|---|---|---|---|---|---|---|
| 0% | 116 ± 5 | 2.8 ± 0.1 | 11.6 ± 0.8 | 27.4 ± 0.3 | 242.3 ± 3.2 | 0.034 ± 0.01 |
| 2% | 127 ± 5 | 3.1 ± 0.1 | 18.9 ± 0.9 | 33.6 ± 0.5 | 466.9 ± 5.7 | 0.038 ± 0.01 |
| 4% | 133 ± 5 | 3.4 ± 0.1 | 19.4 ± 0.9 | 18.7 ± 1.1 | 211.8 ± 2.9 | 0.043 ± 0.01 |
| 6% | 393 ± 9 | 9.6 ± 0.5 | 22.4 ± 1.2 | 9.7 ± 1.2 | 141.2 ± 2.2 | 0.117 ± 0.08 |

tensile strength. Furthermore, $ZrO_2$ can serve as a nucleating agent, promoting PCL crystallinity, which further contributes to mechanical reinforcement. Collectively, these effects dominate over any minor plasticization caused by moisture adsorption, resulting in an overall improvement in the mechanical performance of the nanocomposites. An optimal filler dispersion enabling uniform load distribution.[58] At 4 wt% $ZrO_2$, Young's modulus and UTS remain almost similar and within experimental error to that obtained for 2 wt% $ZrO_2$, as the matrix modulus is already significant (~130 MPa). However, a reduced strain to failure of about 44% for the 4 wt% $ZrO_2$ sample compared to 2 wt% $ZrO_2$. The decreased strain to failure in the 4 wt% sample results from the augmented density of damage initiation sites (originated from adding $ZrO_2$ nanoparticles) combined with significantly increased constraint on plastic matrix deformation due to smaller inter-particle spacing. Moreover, Fig. 3c shows SEM images, where the initiation of agglomeration and clusters of $ZrO_2$ nanoparticles is revealed, which increases the probability of stress concentration and damage initiation sites, providing easier paths for crack propagation and leading to premature fracture. The similar Young's modulus and UTS at 2 wt% and 4 wt% reflects effective reinforcement at both concentrations, with 4 wt% approaching the dispersion limit.[59,60]

However, at 6 wt% $ZrO_2$, UTS, strain to failure, and toughness decline due to nanoparticle agglomeration, which creates stress concentration sites, weakens polymer–polymer chain interactions, and promotes premature brittle fracture. This trade-off is typical in polymer nanocomposites, where high filler content boosts stiffness and strength but compromises ductility, leading to a sudden, catastrophic failure with minimal energy absorption.[61] These findings align with existing literature.[62,63]

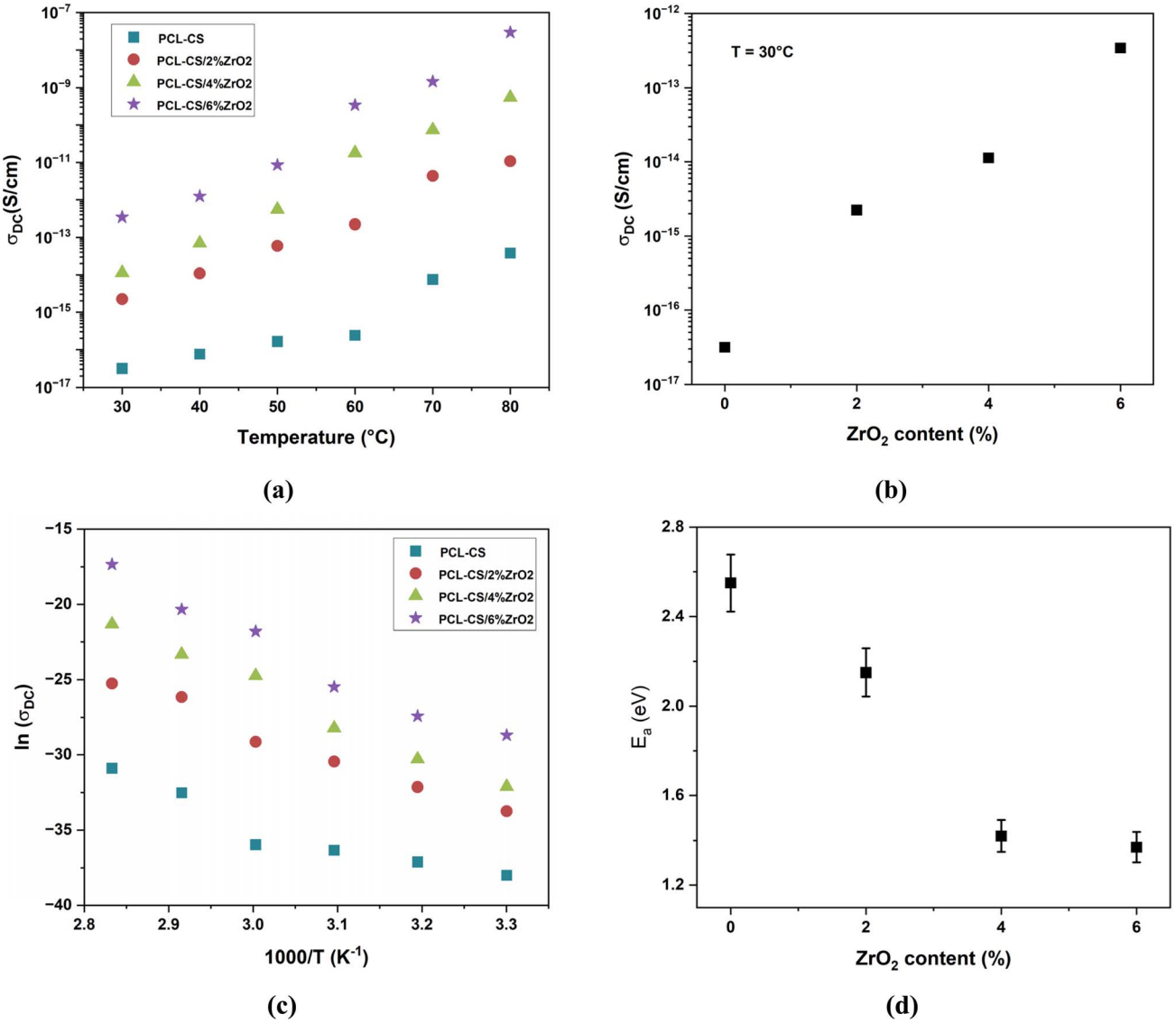


Fig. 5 DC electrical properties of PCL-CS and PCL-CS/$ZrO_2$ nanocomposite films: (a) electrical conductivity with temperature, (b) electrical conductivity with $ZrO_2$ contents, (c) plot of $\ln(\sigma_{DC})$ *versus* inverted absolute temperature, and (d) thermal activation energy.

### 3.5. Electrical and dielectric study

There have been few studies on the direct current (DC) electrical properties of PCL-CS based nanocomposites. However, examining these properties is essential to determine the suitability of such materials for applications such as sensors and actuators. The DC conductivity of PCL-CS copolymer was calculated using eqn (1), and its variation with temperature and $ZrO_2$ content is shown in Fig. 5a and b. The incorporation of $ZrO_2$ nanoparticles significantly enhances the DC electrical conductivity of the PCL-CS copolymer, especially with increasing temperature.

The observed conductivity enhancement is related to the combined effect of increased charge carrier mobility and higher carrier concentration. With increasing temperature and nanoparticle content, the number of charge carriers with higher kinetic energy rises. These carriers undergo thermally activated hopping between localized states, resulting in improved conductivity.[64,65] Furthermore, the incorporation of $ZrO_2$ introduces localized energy levels within the polymer's band gap, which reduces the effective band gap and promotes charge transport. The thermal activation energy of the PCL-CS/$ZrO_2$ nanocomposites is another key parameter used to evaluate how charge carriers overcome energy barriers to contribute to conductivity. This was calculated using eqn (2). The plot of $\ln(\sigma_{DC})$ *versus* $1000/T$ is shown in Fig. 5c. The activation energy values for the PCL-CS/$ZrO_2$ nanocomposites were found to range from 2.55 eV to 1.37 eV, with the highest value observed for pure PCL-CS. As the $ZrO_2$ content increases, the electrical conductivity improves due to greater charge carrier localization and a reduction in activation energy. Fig. 5d illustrates the relationship between thermal activation energy and $ZrO_2$ nanoparticle content. This activation energy decreases as the $ZrO_2$ content increases. This trend is attributed to the formation of localized energy states within the band gap, which act as shallow traps for charge carriers.[66,67] At higher $ZrO_2$ concentrations, the development of a continuous conductive network within the nanocomposite further contributes to the reduction in activation energy by enhancing charge transport pathways.

The AC electrical characteristics of PCL-CS/$ZrO_2$ nanocomposites were investigated, including the dielectric constant, dielectric loss, and AC electrical conductivity within a frequency range of 100 Hz to $5 \times 10^6$ Hz at room temperature. The evolution dielectric constant for PCL-CS/$ZrO_2$ nanocomposites as a function of frequency is shown in Fig. 6a.

A clear decrease in dielectric constant with increasing frequency is observed, attributed to dipole alignment and reduced interfacial polarization under alternating electric fields. This behavior is consistent with studies reported on other nanocomposite systems, such as PCL/$TiO_2$,[68] where high-frequency dipole relaxation similarly dominates over space-charge effects.[69] However, the PCL-CS/$ZrO_2$ system exhibits higher dielectric constant at low frequencies (1 kHz) compared to polybutadiene (PB)/$SiO_2$ composites.[70] Li *et al.*,[71] reported that the improvement in dielectric properties is linked to Maxwell–Wagner–Sillars (MWS) interfacial polarization. This type of polarization occurs due to the accumulation of electric charge at the interfaces between the constituent phases (matrix

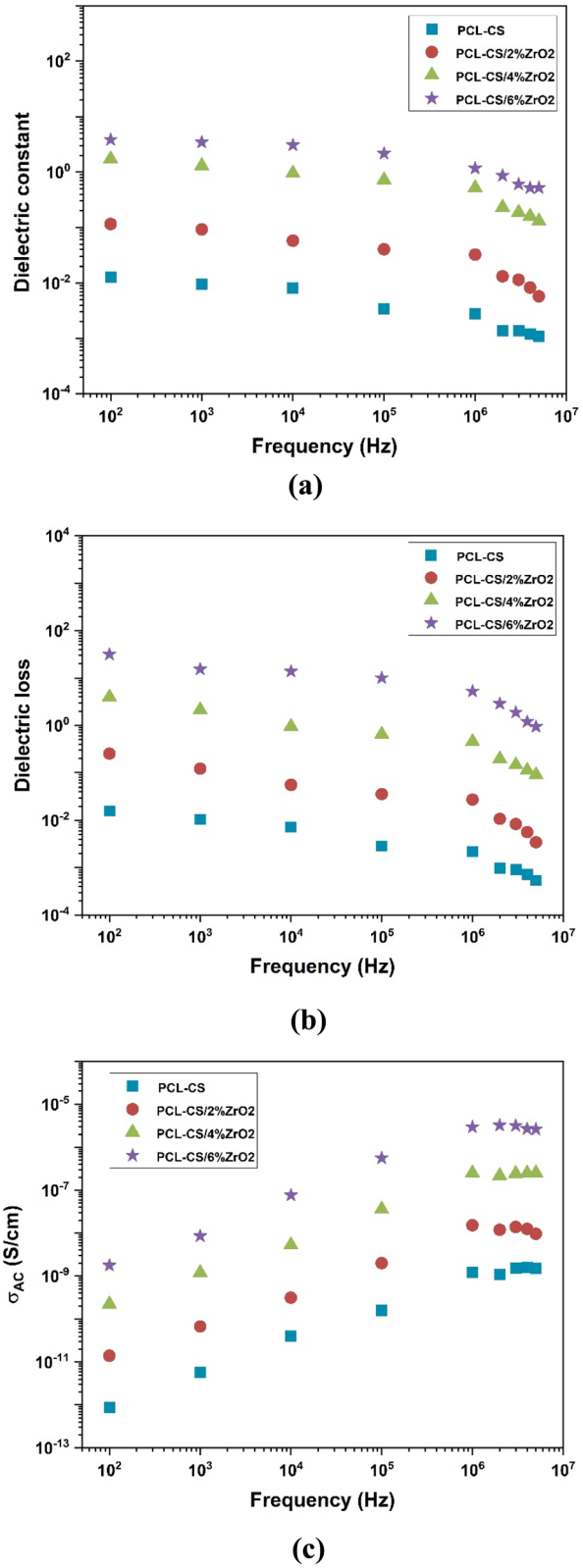


Fig. 6 Dielectric properties for PCL-CS/$ZrO_2$ nanocomposites: (a) dielectric constant, (b) dielectric loss, and (c) AC electrical conductivity.

and filler) of a composite material, driven by disparities in their dielectric response and relaxation times. Moreover, Fernández-Gil *et al.*,[72] explained the increase in low-frequency permittivity of PCL/ZnO composites can be attributed to the MWS effect. In this mechanism, dipole alignment with the electric field results in charge buildup at the interfaces between the polymer and the dispersed particles, acting as small-scale capacitors. At higher frequencies, the dipoles' ability to realign is hindered, leading to a decrease in their polarization contribution and a subsequent reduction in the relative permittivity.

The dielectric loss of PCL-CS/$ZrO_2$ nanocomposites declines at higher frequencies (as shown in Fig. 6b), as dipoles align with the field before its reversal. Indeed, at lower frequencies, this happens because space charge polarization decreases, causing dielectric loss to increase. However, at higher frequencies, dielectric loss is lower because the electric dipoles can orient themselves with the changing electric field. Notably, the dielectric loss of PCL-CS/$ZrO_2$ is lower than PCL/$TiO_2$ at frequencies >1 MHz due to $TiO_2$'s higher ionic polarization losses.[68] Consequently, PCL-CS/$ZrO_2$ nanocomposites demonstrate low energy loss, rendering them potentially useful for microelectronic devices and pressure sensor applications. However, increasing $ZrO_2$ content raises dielectric loss, a trend also observed in PCL/ZnO composites.[72] Furthermore, an increase in $ZrO_2$ concentration corresponded to a rise in dielectric loss, which can be explained by the generation of a larger quantity of charge carriers within the nanocomposites.[35]

High $ZrO_2$ nanoparticle concentration in the PCL-CS forms a conductive network. Fig. 6c shows AC conductivity of these nanocomposites increasing with frequency. This rise is attributed to low-frequency space charge polarization and enhanced charge carrier mobility *via* hopping, which becomes more significant at higher frequencies. This frequency-dependent conductivity is explained by the jump relaxation model,[73] where hopping between localized defect sites increases with frequency, leading to higher conductivity.

The PCL-CS/$ZrO_2$ system achieves $\sigma \approx 10^{-5}$ S cm$^{-1}$ at 5 MHz, surpassing PCL/$TiO_2$ ($\sigma \approx 10^{-7}$ S cm$^{-1}$)[68] but remaining below PCL/graphene oxide ($\sigma \approx 10^{-3}$ S cm$^{-1}$).[74] This positions $ZrO_2$ as a mid-range dielectric filler, ideal for applications requiring moderate conductivity with low loss like sensors.

### 3.6. Optical properties of PCL-CS/$ZrO_2$ nanocomposites

The optical features of PCL-CS/$ZrO_2$ nanocomposites need to be evaluated in order to assess their suitability in optical and protective coating usage. Fig. 7a displays the variation of

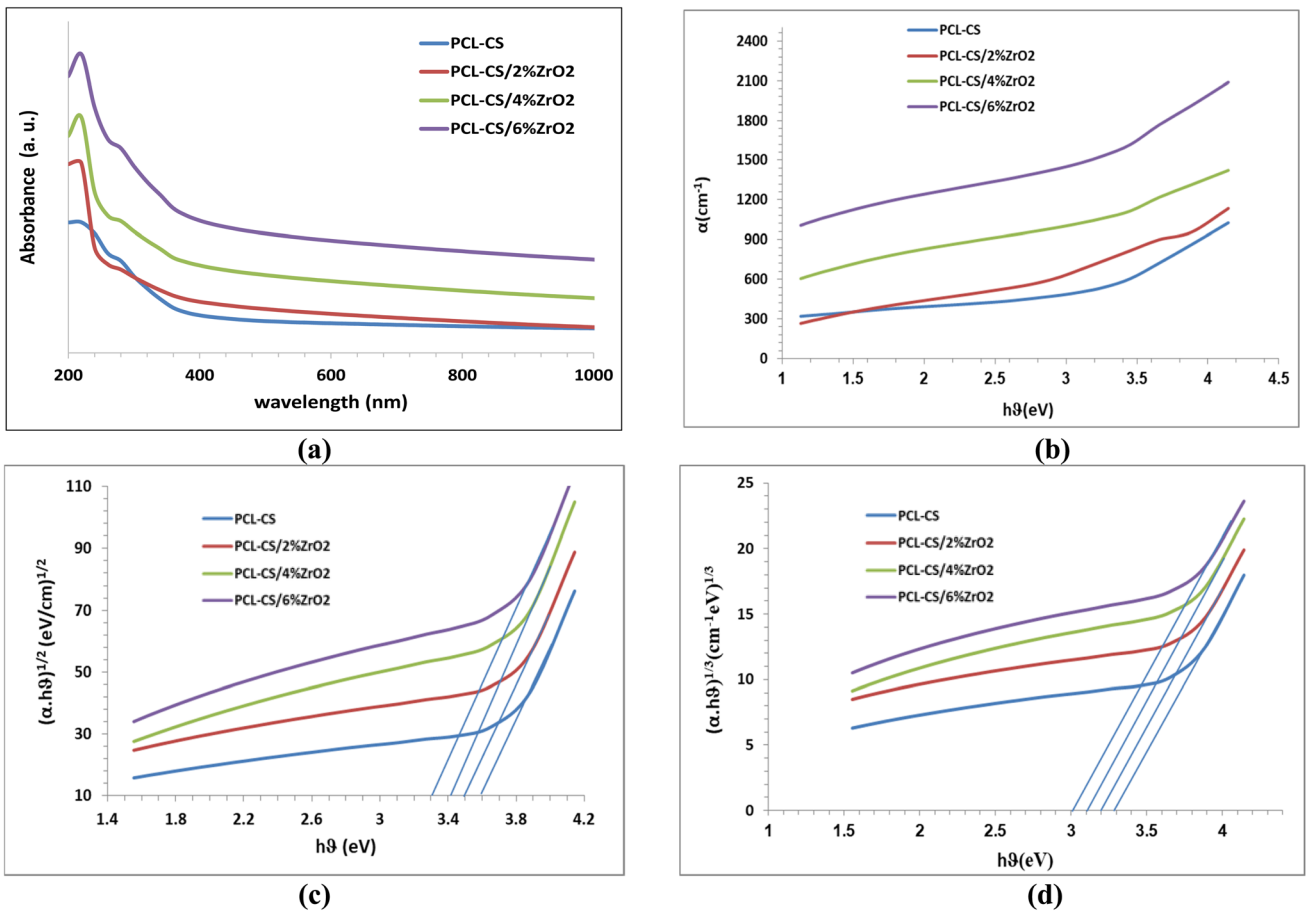


Fig. 7 Optical properties of PCL-CS/$ZrO_2$ nanocomposites: (a) evolution of absorbance along with wavelength, (b) absorption coefficient ($\alpha$), (c) $(\alpha h\nu)^{1/2}$, and (d) $(\alpha h\nu)^{1/3}$ variation as a function of photon energy ($h\nu$).

absorbance for PCL-CS/$ZrO_2$ nanocomposites with wavelength ($\lambda$) of the incident light. The absorbance, ($A$) of nanocomposites increases with the increase of $ZrO_2$ content due to the increase of the number of charge carriers with increasing content of nanoparticles. This behavior is useful for optoelectronics, photocatalysis and solar cells. It is worth noting that the peaks observed around 220 nm in the UV-vis spectra (Fig. 7a) are indeed characteristic absorption bands of the PCL-CS polymer blend itself, primarily attributed to n–π* transitions of the carbonyl groups in PCL and potentially some contributions from the chitosan backbone. These are intrinsic absorption features of the polymers.[75,76]

In general, it is observed that the absorbance decreases with the increasing wavelength for all prepared nanocomposites. This perspective, physically means that an incident photon has not been able to excite the electron and move it from a lower to a higher energy level because the energy of the incident photon is less than the value of the energy gap of the nanocomposites.[77,78] In the UV-region, the absorbance of all samples of nanocomposites has a high value, this is due to the excitations of donor level electrons to the conduction band at these energies. In accordance with the eqn (6), the absorption coefficient ($\alpha$) of PCL-CS/$ZrO_2$ nanocomposites were measured as a function of the photon energy of the incident light, as shown in Fig. 7b. The absorption coefficient of all prepared nanocomposites increases with increasing energy of the incident photon. This means that the electron transition has a high probability; *i.e.*, the energy of the incident photon is sufficient to interact with atoms. The absorption coefficient helps to know the electron transition nature. The transition of electrons occurs indirectly when the absorption coefficient of nanocomposite is low at lower energy (*e.g.*, $\alpha < 10^4$ $cm^{-1}$). On the other hand, higher absorption coefficient with higher energy ($\alpha > 10^4$ $cm^{-1}$) results in direct electrons' transition.[79] Our findings reveal that the absorption coefficient value of PCL-CS/$ZrO_2$ nanocomposites is lower than $10^4$ $cm^{-1}$ which means the transition of electrons is indirect. For PCL-CS/$ZrO_2$ nanocomposites, $E_g^{opt}$ is determined by plotting $(\alpha h\nu)^{1/2}$ as a function of ($h\nu$) and extrapolating the straight-line portion to intersect with the $x$-axis which gives the energy gap value for nanocomposites, as shown in Fig. 7c and d. Table 2 indicates that the indirect energy gap decreases as $ZrO_2$ content increases. At higher $ZrO_2$ concentrations, the transition of electrons from the valence band to local energy levels and subsequently to the conduction band creates localized states within the forbidden energy gap.[80] The observed reduction in optical band gap of PCL-CS/$ZrO_2$ nanocomposites arises from a synergistic combination of interfacial interactions and intrinsic material defects, with interfacial charge transfer processes serving as the dominant mechanism. The formation of a heterogeneous interphase between the PCL-CS polymer matrix and $ZrO_2$ nanoparticles creates new electronic states at the interface through energy level alignment. These interfacial states act as stepping stones for electron transitions, effectively reducing the energy required for optical excitation and thus narrowing the apparent band gap.[81] This mechanism is strongly supported by FTIR evidence showing strong chemical interactions between PCL-CS and $ZrO_2$, along with mechanical property enhancements that confirm effective interfacial bonding.[82,83] Complementing this primary mechanism, oxygen vacancies and other intrinsic defects in $ZrO_2$ nanoparticles, such as $Zr^{4+}$ centers introduce localized energy levels within the band gap, contributing to sub-bandgap absorption and further band gap reduction as defect concentration increases with nanoparticle loading.[84,85] While quantum confinement effects are typically significant for semiconductor nanoparticles below 10 nm, our $ZrO_2$ nanoparticles with 100 nm average diameter are too large to exhibit substantial quantum confinement, making surface area and dispersion effects more relevant than size-induced electronic modifications.[86]

Table 2 Optical band gap allowed and forbidden for PCL-CS/$ZrO_2$ nanocomposites

| Samples | $E_g^{opt}$ allowed (eV) | $E_g^{opt}$ forbidden (eV) |
|---|---|---|
| PCL-CS | 3.59 ± 0.03 | 3.28 ± 0.03 |
| PCL-CS/2%$ZrO_2$ | 3.50 ± 0.03 | 3.21 ± 0.03 |
| PCL-CS/4%$ZrO_2$ | 3.43 ± 0.03 | 3.10 ± 0.03 |
| PCL-CS/6%$ZrO_2$ | 3.32 ± 0.03 | 3.02 ± 0.03 |

Fig. 8a shows the refractive index of PCL-CS/$ZrO_2$ nanocomposites as a function of wavelength. The results reveal that the refractive index increases with both the wavelength of the incident light and the $ZrO_2$ content. This behavior is attributed to the high absorbance of the nanocomposites, which decreases reflection and transmission, making them advantageous for optical applications.[87] These findings align with the results of Alsaad *et al.*[88] who obtained an increase of the refractive index of the PMMA-PVA/$TiO_2$ nanocomposite films. They attributed this increase to the condensation of smaller nanoparticles into larger clusters. Fig. 8b shows how the extinction coefficient of PCL-CS/$ZrO_2$ nanocomposites varies with wavelength. This is because as the $ZrO_2$ concentration increases, both optical absorption and photon dispersion in the PCL-CS composite also increase. Higher $ZrO_2$ concentrations are accompanied by an increase in the extinction coefficient. This property may be attributed to the high absorbance of the nanocomposite samples, which results in a higher extinction coefficient at UV wavelengths. Since the nanocomposites' absorption coefficient remains almost constant from the visible to the near-infrared region, the extinction coefficient likewise increases with increasing wavelength.[89] Fig. 8c displays the variation of the real part of dielectric constant ($\varepsilon_r$) along with the wavelength for PCL-CS/$ZrO_2$ nanocomposites. The trend of the real part of the dielectric constant is similar to that of the refractive index because, according to the eqn (10), the value of the extinction coefficient square ($k^2$) is very small compared with the refractive index square ($n^2$). The real part of the dielectric constant of PCL-CS composite is increased at higher $ZrO_2$ content due to the decrease of the scattering of the incident photon. The impact of $ZrO_2$ nanoparticles on the imaginary part of dielectric constant ($\varepsilon_i$) is shown in Fig. 8d. According to the eqn (11), the imaginary part of the dielectric constant is essentially proportional with extinction coefficient values. The imaginary part of the

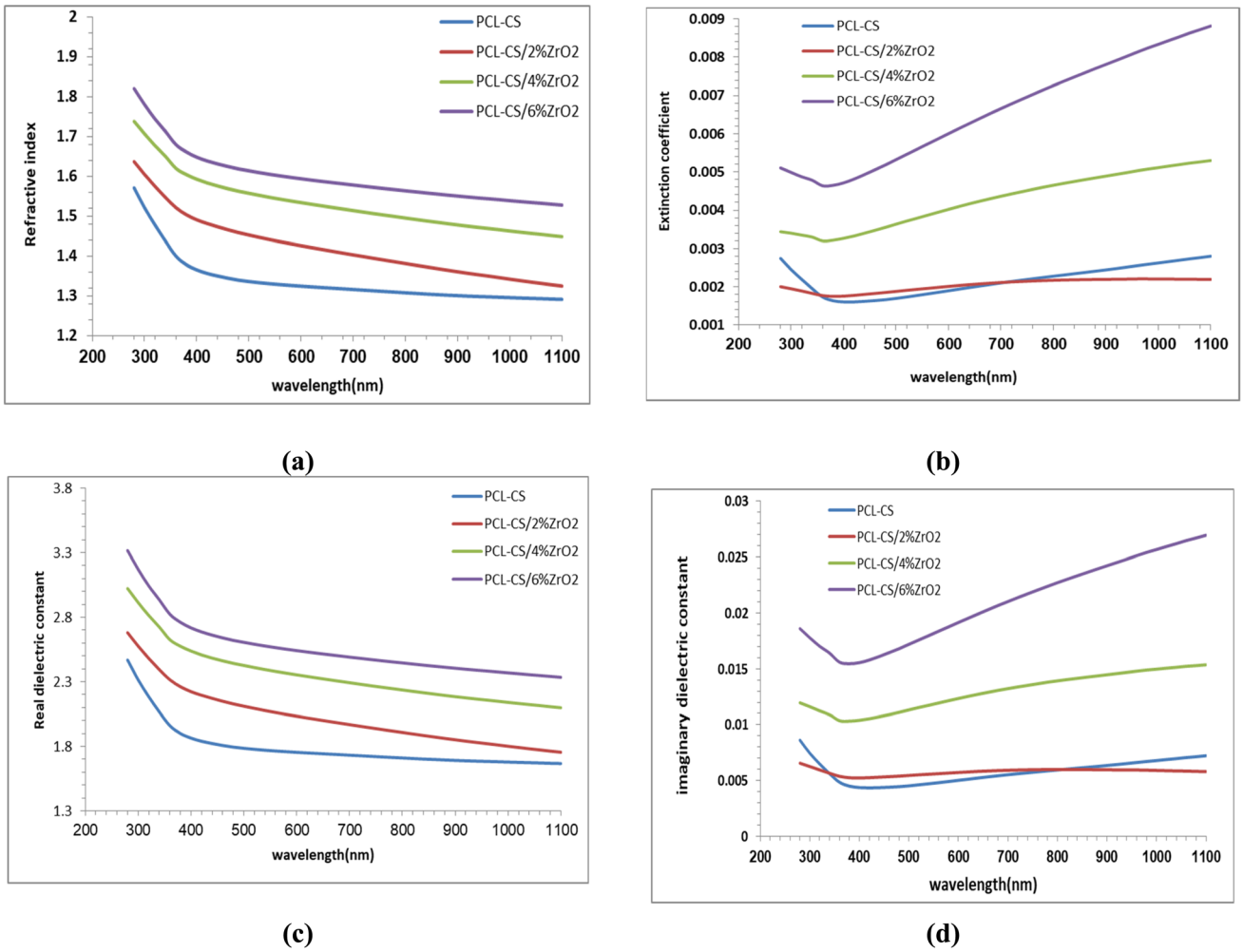


Fig. 8 Optical properties of PCL-CS/$ZrO_2$ nanocomposites: (a) refractive index, (b) extinction coefficient, (c) real part of dielectric constant, and (d) imaginary part for dielectric constant.

dielectric constant of nanocomposites is increased with the increasing of nanoparticles contents because of increased absorption coefficient of nanocomposites. These results are in good agreement with the literature.[25]

The unique capability to precisely tune the optical absorbance, band gap, and refractive index of $ZrO_2$-polymer nanocomposite films by adjusting $ZrO_2$ nanoparticle loading makes these materials versatile for flexible optoelectronic applications, including transparent electrodes, optical sensors, and protective display coatings.[90] For example, increasing $ZrO_2$ content from 2 wt% to 4 wt% has been demonstrated to systematically decrease the optical band gap and enhance the refractive index, enabling fine control over transparency and light management to suit specific device requirements.[91] Highly transparent and flexible PCL-CS/$ZrO_2$ films, achieving refractive indices up to 1.70 while maintaining highly visible-light transmittance, even at higher nanoparticle concentrations, highlighting their suitability for advanced photonic and optoelectronic devices.[91] Moreover, uniform dispersion of $ZrO_2$ nanoparticles in PCL-CS films yields nanocomposite films with outstanding transparency and dielectric performance, positioning them as promising candidates for next-generation smart windows, touch screens, and sensors.[92,93] Therefore, by selecting an optimal $ZrO_2$ concentration, such as 2 wt% or 4 wt%, the material's optical and electronic properties can be tailored for specific applications, as demonstrated in prototype transparent electronics and flexible optoelectronic platforms.[94,95]

### 3.7. Antibacterial activity

Bacterial infections in orthopedic implants are a primary cause of delayed bone tissue recovery and implant failure.[96] Consequently, developing functional materials that inhibit bacterial growth while supplying essential elements for healing is essential.[97] In this study, Gram-negative *Escherichia coli* (*E. coli*) and Gram-positive *Staphylococcus aureus* (*S. aureus*) were used as model organisms to evaluate the antibacterial properties of PCL-CS/$ZrO_2$ nanocomposites against bacterial infections.

Fig. 9 shows the antibacterial activity of the PCL-CS/$ZrO_2$ nanocomposites. Fig. 9a displays the inhibition zones, which clearly increase in diameter against both *S. aureus* (Gram-positive) and *E. coli* (Gram-negative) as the $ZrO_2$ content rises. Fig. 9b quantifies the diameter of these inhibition zones after

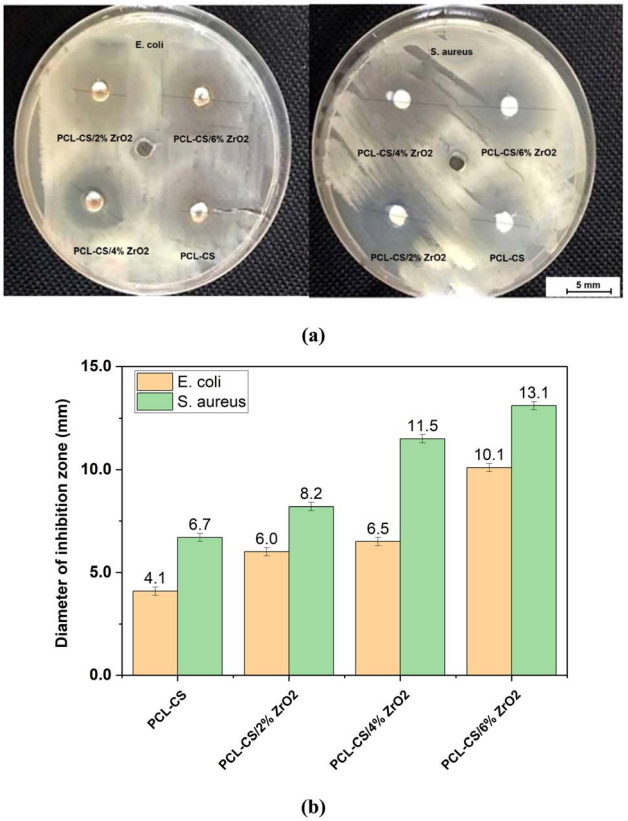


Fig. 9 Antibacterial behavior of CS-PCL/$ZrO_2$ nanocomposites against the bacteria strains of *E. coli* and *S. aureus*: (a) optigat image of agar plates and (b) diameter inhibition zone for each nanocomposite content.

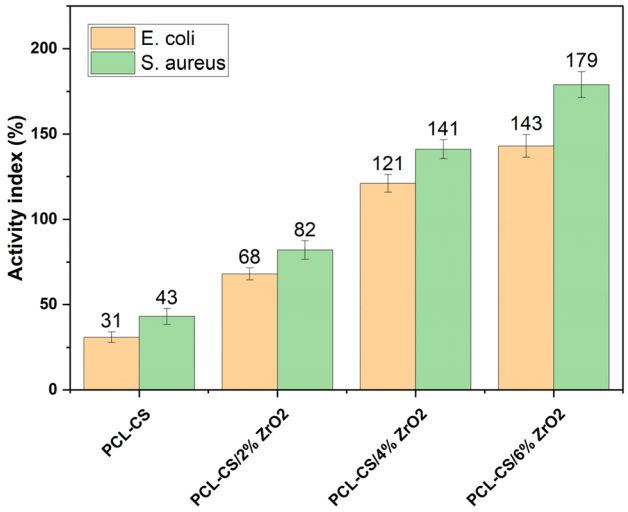


Fig. 10 Antibacterial activity index of PCL-CS/$ZrO_2$ nanocomposite films.

an incubation of 24 hours. Notably, the diameter inhibition zones against *S. aureus* ranges from 6.7 mm to 13.1 mm, outperforming those against *E. coli*, which increases from 4.1 mm to 10.1 mm. Compared to the neat PCL-CS sample, the PCL-Cs/$ZrO_2$ samples exhibit significantly larger inhibition zones, with the diameter increasing as the $ZrO_2$ concentration rises.

These findings aligned with observations previously noted by Ghasemian Lemraski *et al.*[98] who investigated the antibacterial characteristics of CS-PVA/Cu nanocomposites, and found a diameter of inhibition zones of (15.6 ± 1.1) mm for *S. aureus* and (13.3 ± 0.8) mm for *E. coli*. Moreover, Kahdim *et al.*[38] studied the impact of Nigella sativa on the antimicrobial properties of PCL-CS, and obtained 7.4 mm for *E. coli* and 8.0 mm for *S. aureus*. Fig. 10 presents the antibacterial activity index (%) index[99] of PCL-CS/$ZrO_2$ nanocomposites against *S. aureus* and *E. coli* across varying $ZrO_2$ concentrations: 0 wt% (PCL-CS), 2 wt% $ZrO_2$, 4 wt% ($ZO_2$), and 6 wt% ($ZrO_2$). Results reveal a progressive increase in antibacterial activity with rising $ZrO_2$ content, highlighting the efficacy of $ZrO_2$ as an antibacterial agent within the PCL-CS copolymer. The baseline activity at 0 wt% (43% for *S. aureus*, 31% for *E. coli*) is attributable to chitosan's cationic properties, which disrupt bacterial membranes. Incorporation of 2 wt% $ZrO_2$ significantly enhanced the activity to 81.8% for *S. aureus* and 68% for *E. coli*, suggesting optimal nanoparticle dispersion. The activity peaked at 4 wt% (141% for *S. aureus*, 121% for *E. coli*), with a maximum of 179% for *S. aureus* and 143% for *E. coli* at 6 wt%, despite nanoparticle agglomeration as revealed in SEM image (Fig. 3d). This trend indicates a synergistic effect between chitosan and $ZrO_2$, with *S. aureus* exhibiting greater susceptibility, attributed to its Gram-positive structure.

This robust antibacterial effect can be attributed to both physical and chemical mechanisms. Physically, the sharp edges of $ZrO_2$ nanoparticles can mechanically disrupt bacterial cell walls.[100] Chemically, the production of reactive oxygen species (ROS), such as hydrogen peroxide ($H_2O_2$), hydroxyl radicals ($OH^-$) and superoxide anions, and the release of $Zr^{4+}$ ions from $ZrO_2$ nanoparticles play an important role. These compounds and ions interact with bacterial cell walls and internal components, such as proteins and carbohydrates, leading to elevated bacterial mortality.[99,101] According to Tabassum *et al.*,[100] metal oxides tend to carry a positive charge, while microorganisms typically exhibit a negative charge. This difference in surface charge leads to electrostatic attraction between the metal oxide nanoparticles and the microorganisms. The resulting interaction can induce oxidation processes in microorganisms, ultimately leading to their demise. The observed differences in activity index between Gram-positive and Gram-negative bacteria may stem from their structural distinctions. Indeed, Gram-negative bacteria exhibit greater resistance due to their dual-layered cell membranes, in contrast to the single-layered membranes of Gram-positive bacteria.[38] Gram-negative bacteria possess a complex cell envelope featuring an inner cytoplasmic membrane, a thin peptidoglycan layer, and an outer membrane rich in lipopolysaccharides that act as a barrier, which may limit $ZrO_2$ nanoparticle penetration.[102] While the electrostatic attraction between positively charged $Zr^{4+}$ ions and the negatively charged cell walls of Gram-negative bacteria can enhance nanoparticle penetration and improve the PCL-CS composite's antibacterial efficacy against them,[103] Gram-positive bacteria (*S. aureus*) demonstrate even greater susceptibility. This is attributed to their simpler cell wall

structure, which lacks the outer protective barrier found in Gram-negative strains.[38] These findings suggest that PCL-CS/$ZrO_2$ nanocomposites exhibit remarkable antimicrobial properties, making them promising candidates for applications in food packaging and medical devices, where safety and hygiene are paramount.[99]

## 4. Conclusions

This study successfully developed and characterized novel multifunctional nanocomposite films composed of PCL, CS, and $ZrO_2$ nanoparticles, addressing the vital need for sustainable materials with advanced properties. The comprehensive investigation unequivocally demonstrated that the incorporation of $ZrO_2$ significantly enhances the mechanical, electrical, optical, and antibacterial performance of the PCL-CS copolymer. Specifically, mechanical analysis revealed that the addition of 2 wt% $ZrO_2$ yielded an optimal balance of mechanical properties, resulting in a notable 63% increase in UTS and a 93% increase in toughness compared to neat PCL-CS. While higher $ZrO_2$ concentrations, such as 6 wt%, achieved the highest Young's modulus (393 MPa) and UTS (22.4 MPa), this was accompanied by a reduction in ductility. Electrically, the nanocomposites exhibited significantly enhanced DC conductivity with increasing $ZrO_2$ content and temperature, alongside improved dielectric characteristics, with the thermal activation energy decreasing from 2.55 eV for neat PCL-CS to 1.37 eV for the 6 wt% $ZrO_2$ nanocomposite. Optically, the films' absorbance, energy gap, and refractive index were effectively tuned by varying $ZrO_2$ concentrations, with the indirect energy gap decreasing from 3.28 eV to 3.02 eV as $ZrO_2$ content increased, indicating their suitability for diverse optical applications. Furthermore, a key finding was the remarkable antibacterial efficacy of these nanocomposites against both Gram-positive *S. aureus* and Gram-negative *E. coli*. The inhibition zone diameters increased with $ZrO_2$ content, reaching up to 13.1 mm for *S. aureus* and 10.1 mm for *E. coli*, and the antibacterial activity index increased significantly, demonstrating a synergistic effect between chitosan and $ZrO_2$.

Finally, the multifunctionality of the developed PCL-CS/$ZrO_2$ nanocomposite films renders them highly suitable for a broad spectrum of advanced applications, including, but not limited to, biomedical devices, flexible optoelectronics, and smart packaging. The optimal nanocomposite composition depends on the desired application, with 2 wt% $ZrO_2$ offering the best balance of mechanical properties, while higher concentrations (*e.g.*, 6 wt%) maximize electrical, optical, and antibacterial performance despite some mechanical trade-offs. Future research endeavors could focus on further optimizing nanoparticle dispersion at higher concentrations and exploring long-term *in vivo* performance to fully realize their potential in practical applications.

## Author contributions

Qasim Shakir Kahdim: writing—original draft preparation, writing—review and editing, conceptualization, methodology, investigation, data curation, validation, resources, formal analysis, visualization. Zohra Benzarti: writing—original draft preparation, writing—review and editing, methodology, investigation, data curation, validation, resources, formal analysis, visualization, supervision. Mohanad H. Mousa: writing—original draft preparation, writing—review and editing, conceptualization, methodology, investigation, data curation, validation, formal analysis, visualization. Maher Hassan Rasheed: writing—original draft preparation, conceptualization, methodology, investigation, data curation, validation, formal analysis, visualization. Najmeddine Abdelmoula: writing—original draft preparation, writing—review and editing, methodology, data curation, validation, formal analysis, visualization, supervision. Ali Khalfallah: writing—original draft preparation, writing—review and editing, methodology, validation, formal analysis, visualization, data curation.

## Conflicts of interest

There are no conflicts to declare.

## Data availability

All data for this study—including figures, tables, and any supporting details—are contained within the main article.

## Acknowledgements

Zohra Benzarti gratefully acknowledges support from project no 7225-ILLIANCE High Performing Energy, Project supported by the RRP-Recovery and Resilience Plan and the European NextGeneration EU Funds, following the AVISON. 02/C05-i01/2022, Component 5, Capitalization and Business Innovation, Mobilizing Agendas for Business Innovation. She and Ali Khalfallah also acknowledge support from national funds through FCT- Foundation for Science and Technology, under project UID/00285, Centre for Mechanical Engineering, Materials and Processes, and LA/P/0112/2020.

## References

1 B. Mishra, J. Panda, A. K. Mishra, P. C. Nath, P. K. Nayak, U. Mahapatra, M. Sharma, H. Chopra, Y. K. Mohanta and K. Sridhar, Recent Advances in Sustainable Biopolymer-Based Nanocomposites for Smart Food Packaging: A Review, *Int. J. Biol. Macromol.*, 2024, **279**, 135583, DOI: 10.1016/j.ijbiomac.2024.135583.

2 A. Samir, F. H. Ashour, A. A. A. Hakim and M. Bassyouni, Recent Advances in Biodegradable Polymers for Sustainable Applications, *npj Mater. Degrad.*, 2022, **6**, 68, DOI: 10.1038/s41529-022-00277-7.

3 M. H. Mousa, Y. Dong and I. J. Davies, Recent Advances in Bionanocomposites: Preparation, Properties, and Applications, *Int. J. Polym. Mater. Polym. Biomater.*, 2016, **65**, 225–254, DOI: 10.1080/00914037.2015.1103240.

4 N. Peidavosi, M. Azami, N. Beheshtizadeh and A. Ramazani Saadatabadi, Piezoelectric Conductive Electrospun

Nanocomposite PCL/Polyaniline/Barium Titanate Scaffold for Tissue Engineering Applications, *Sci. Rep.*, 2022, **12**, 20828, DOI: 10.1038/s41598-022-25332-w.

5 M. Laubach, P. Kobbe and D. W. Hutmacher, Biodegradable Interbody Cages for Lumbar Spine Fusion: Current Concepts and Future Directions, *Biomaterials*, 2022, **288**, 121699, DOI: 10.1016/j.biomaterials.2022.121699.

6 M. Mohammadi Zerankeshi, R. Bakhshi and R. Alizadeh, Polymer/Metal Composite 3D Porous Bone Tissue Engineering Scaffolds Fabricated by Additive Manufacturing Techniques: A Review, *Bioprinting*, 2022, **25**, e00191, DOI: 10.1016/j.bprint.2022.e00191.

7 S. Sahoo, A. Sasmal, R. Nanda, A. R. Phani and P. L. Nayak, Synthesis of Chitosan–Polycaprolactone Blend for Control Delivery of Ofloxacin Drug, *Carbohydr. Polym.*, 2010, **79**, 106–113, DOI: 10.1016/j.carbpol.2009.07.042.

8 Q. Cai, J. Bei and S. Wang, Synthesis and Degradation of a Tri-Component Copolymer Derived from Glycolide, L-Lactide, and ε-Caprolactone, *J. Biomater. Sci., Polym. Ed.*, 2000, **11**, 273–288, DOI: 10.1163/156856200743698.

9 D. S. Hubbell and S. L. Cooper, The Physical Properties and Morphology of Poly-ε-Caprolactone Polymer Blends, *J. Appl. Polym. Sci.*, 1977, **21**, 3035–3061, DOI: 10.1002/app.1977.070211117.

10 M. Azmana, S. Mahmood, A. R. Hilles, A. Rahman, M. A. B. Arifin and S. Ahmed, A Review on Chitosan and Chitosan-Based Bionanocomposites: Promising Material for Combatting Global Issues and Its Applications, *Int. J. Biol. Macromol.*, 2021, **185**, 832–848, DOI: 10.1016/j.ijbiomac.2021.07.023.

11 C. Cui, S. Sun, S. Wu, S. Chen, J. Ma and F. Zhou, Electrospun Chitosan Nanofibers for Wound Healing Application, *Eng. Regener.*, 2021, **2**, 82–90, DOI: 10.1016/j.engreg.2021.08.001.

12 Y. A. A. Alghuwainem, M. Gouda, M. M. Khalaf, A. Elmushyakhi, M. F. Abou Taleb and H. M. A. El-Lateef, Synthesis and Characterization of Chitosan-Containing ZnS/ZrO2/Graphene Oxide Nanocomposites and Their Application in Wound Dressing, *Polymers*, 2022, **14**, 5195, DOI: 10.3390/polym14235195.

13 D. de Cassan, A. Becker, B. Glasmacher, Y. Roger, A. Hoffmann, T. R. Gengenbach, C. D. Easton, R. Hänsch and H. Menzel, Blending Chitosan-g-poly(Caprolactone) with Poly(Caprolactone) by Electrospinning to Produce Functional Fiber Mats for Tissue Engineering Applications, *J. Appl. Polym. Sci.*, 2020, **137**(18), 48650, DOI: 10.1002/app.48650.

14 A. Sarasam and S. Madihally, Characterization of Chitosan–Polycaprolactone Blends for Tissue Engineering Applications, *Biomaterials*, 2005, **26**, 5500–5508, DOI: 10.1016/j.biomaterials.2005.01.071.

15 T. J. Wang, I. J. Wang, J. N. Lu and T. H. Young, Novel Chitosan-Polycaprolactone Blends as Potential Scaffold and Carrier for Corneal Endothelial Transplantation, *Mol. Vision*, 2012, **18**, 255–264.

16 M. Kaur, A. Sharma, V. Puri, G. Aggarwal, P. Maman, K. Huanbutta, M. Nagpal and T. Sangnim, Chitosan-Based Polymer Blends for Drug Delivery Systems, *Polymers*, 2023, **15**, 2028, DOI: 10.3390/polym15092028.

17 M. Fadaie, E. Mirzaei, B. Geramizadeh and Z. Asvar, Incorporation of Nanofibrillated Chitosan into Electrospun PCL Nanofibers Makes Scaffolds with Enhanced Mechanical and Biological Properties, *Carbohydr. Polym.*, 2018, **199**, 628–640, DOI: 10.1016/j.carbpol.2018.07.061.

18 A. R. Sarasam, R. K. Krishnaswamy and S. V. Madihally, Blending Chitosan with Polycaprolactone: Effects on Physicochemical and Antibacterial Properties, *Biomacromolecules*, 2006, **7**, 1131–1138, DOI: 10.1021/bm050935d.

19 D. Poddar, M. Majood, A. Singh, S. Mohanty and P. Jain, Chitosan-Coated Pore Wall Polycaprolactone Three-Dimensional Porous Scaffolds Fabricated by Porogen Leaching Method for Bone Tissue Engineering: A Comparative Study on Blending Technique to Fabricate Scaffolds, *Prog. Biomater.*, 2021, **10**, 281–297, DOI: 10.1007/s40204-021-00172-5.

20 Y. Li, H. Cheng, M. Yu, C. Han and H. Shi, Blends of Biodegradable Poly(ε-Caprolactone) and Sustainable Poly(Propylene Carbonate) with Enhanced Mechanical and Rheological Properties, *Colloid Polym. Sci.*, 2022, **300**, 59–68, DOI: 10.1007/s00396-021-04931-5.

21 A. M. Abdelghany, M. S. Meikhail and W. M. Awad, Electrical Conductivity of Chitosan/PCL Hosting Network for CdSe Quantum Dots, *Polym. Bull.*, 2022, **79**, 4381–4393, DOI: 10.1007/s00289-021-03715-9.

22 M. Shelly, M. Mathew, P. P. Pradyumnan and T. Francis, Dielectric and Thermal Stability Studies on High Density Polyethylene – Chitosan Composites Plasticized with Palm Oil, *Mater. Today: Proc.*, 2021, **46**, 2742–2746, DOI: 10.1016/j.matpr.2021.02.479.

23 B. Mutlu, S. Çaylak and Ş. Duman, Incorporation of Cerium Oxide into Hydroxyapatite/Chitosan Composite Scaffolds for Bone Repair, *Process. Appl. Ceram.*, 2022, **16**, 207–217, DOI: 10.2298/PAC2203207M.

24 B. T. Gebretsadik and A. N. Ali, Nanofillers Tailored Polymers and Enhanced Synergistic Properties for Engineering Applications: A Review, *J. Polym. Res.*, 2024, **31**, 314, DOI: 10.1007/s10965-024-04165-3.

25 J. Xie, Z. Zhu, H. Tao, S. Zhou, Z. Liang, Z. Li, R. Yao, Y. Wang, H. Ning and J. Peng, Research Progress of High Dielectric Constant Zirconia-Based Materials for Gate Dielectric Application, *Coatings*, 2020, **10**, 698, DOI: 10.3390/coatings10070698.

26 J. Liu, J. Li, J. Wu and J. Sun, Structure and Dielectric Property of High-k ZrO2 Films Grown by Atomic Layer Deposition Using Tetrakis(Dimethylamido)Zirconium and Ozone, *Nanoscale Res. Lett.*, 2019, **14**, 154, DOI: 10.1186/s11671-019-2989-8.

27 Q.-Q. Liu, Q.-H. Lin, X.-D. Qi, N. Zhang, T. Huang, J.-H. Yang and Y. Wang, Significantly Enhanced Energy Storage Performances of PEI-Based Composites Utilizing Surface Functionalized ZrO2 Nanoparticles for High-

Temperature Application, *Chin. J. Polym. Sci.*, 2024, **42**, 322–332, DOI: 10.1007/s10118-024-3068-x.

28 A. Kumar, C. Guo, G. Sharma, D. Pathania, M. Naushad, S. Kalia and P. Dhiman, Magnetically Recoverable ZrO2/Fe3O4/Chitosan Nanomaterials for Enhanced Sunlight Driven Photoreduction of Carcinogenic Cr( vi ) and Dechlorination & Mineralization of 4-Chlorophenol from Simulated Waste Water, *RSC Adv.*, 2016, **6**, 13251–13263, DOI: 10.1039/C5RA23372K.

29 J. Zhang, F. Zhi, W. Hou, L. Zhang, T. Huo, R. Gu, R. Fan, X. Wang, G. Ren, H. Wang, *et al.*, Magnetic Chitosan/ZrO 2 Composites for Vanadium(V) Adsorption While Concurrently Being Transformed to a Dual Functional Catalyst, *Chem.–Eur. J.*, 2024, **30**(57), e202402450, DOI: 10.1002/chem.202402450.

30 M. Catauro, F. Bollino, P. Veronesi and G. Lamanna, Influence of PCL on Mechanical Properties and Bioactivity of ZrO2-Based Hybrid Coatings Synthesized by Sol–Gel Dip Coating Technique, *Mater. Sci. Eng., C*, 2014, **39**, 344–351, DOI: 10.1016/j.msec.2014.03.025.

31 B. K. Shanmugam, S. Rangaraj, K. Subramani, S. Srinivasan, N. Kandhasamy, K. Arumugam, M. Periyasamy, W. K. Aicher and R. Venkatachalam, Biomimetic Development of Chitosan and Sodium Alginate-based Nanocomposites Contains Zirconia for Tissue Engineering Applications, *J. Biomed. Mater. Res., Part B*, 2022, **110**, 1942–1955, DOI: 10.1002/jbm.b.35052.

32 M. H. Rasheed, Q. S. Kadhim, A. A. Mohaimeed and R. J. Alsaedi, Synthesis and Evaluation Structural, Thermal and Electrical Properties for PCL/TiO2 Nanocomposites, *Trans. Electr. Electron. Mater.*, 2025, **26**, 37–47, DOI: 10.1007/s42341-024-00571-y.

33 S. Hajer, O. Khaldi, A. Dahri, N. Abdelmoula, I. Hammami, M. Pedro Fernandes Graça and Z. Benzarti, Influence of (Co+Al) Co-doping on Structural, Micro-Structural, Optical and Electrical Properties of Nanostructured Zinc Oxide, *Ceram. Int.*, 2024, **50**, 44151–44164, DOI: 10.1016/j.ceramint.2024.08.264.

34 A. Hashim, A. J. Kadham Algidsawi, H. Ahmed, A. Hadi and M. A. Habeeb, Structural, Dielectric, and Optical Properties for (PVA/PVP/CuO) Nanocomposites for Pressure Sensors, *Nanosist., Nanomater., Nanotekhnol.*, 2021, **19**, 91–102, DOI: 10.15407/nnn.19.01.091.

35 A. Hashim and A. Hadi, Synthesis and Characterization of Novel Piezoelectric and Energy Storage Nanocompo-Sites: Biodegradable Materials–Magnesium Oxide Nanoparticles, *Ukr. J. Phys.*, 2017, **62**, 1050–1056, DOI: 10.15407/ujpe62.12.1050.

36 A. Hashim, M. A. Habeeb, A. Khalaf and A. Hadi, Fabrication of (PVA-PAA) Blend-Extracts of Plants Bio-Composites and Studying Their Structural, Electrical and Optical Properties for Humidity Sensors Applications, *Sens. Lett.*, 2017, **15**, 589–596, DOI: 10.1166/sl.2017.3856.

37 A. Mohammad Karim and H. P. Kavehpour, Effect of Viscous Force on Dynamic Contact Angle Measurement Using Wilhelmy Plate Method, *Colloids Surf., A*, 2018, **548**, 54–60, DOI: 10.1016/j.colsurfa.2018.03.058.

38 Q. S. Kahdim, N. Abdelmoula, H. Al-Karagoly, S. Albukhaty and J. Al-Saaidi, Fabrication of a Polycaprolactone/Chitosan Nanofibrous Scaffold Loaded with Nigella Sativa Extract for Biomedical Applications, *Biotechnology*, 2023, **12**, 19, DOI: 10.3390/biotech12010019.

39 C. Rosca, M. I. Popa, G. Lisa and G. C. Chitanu, Interaction of Chitosan with Natural or Synthetic Anionic Polyelectrolytes. 1. The Chitosan–Carboxymethylcellulose Complex, *Carbohydr. Polym.*, 2005, **62**, 35–41, DOI: 10.1016/j.carbpol.2005.07.004.

40 G. Hao, Y. Hu, L. Shi, J. Chen, A. Cui, W. Weng and K. Osako, Physicochemical Characteristics of Chitosan from Swimming Crab (Portunus Trituberculatus) Shells Prepared by Subcritical Water Pretreatment, *Sci. Rep.*, 2021, **11**, 1646, DOI: 10.1038/s41598-021-81318-0.

41 N. Doostmohammadi, M. Yousefpour, M. S. Nourbakhsh and M. Bahraminasab, Fabrication and Characterization of 3D Printed PCL/ZrO2/FA Scaffolds for Bone Tissue Engineering, *Mater. Chem. Phys.*, 2025, **338**, 130659, DOI: 10.1016/j.matchemphys.2025.130659.

42 P. R. Rauta, P. Manivasakan, V. Rajendran, B. B. Sahu, B. K. Panda and P. Mohapatra, Phase Transformation of ZrO2 Nanoparticles Produced from Zircon, *Phase Transitions*, 2012, **85**, 13–26, DOI: 10.1080/01411594.2011.619698.

43 I.-C. Mirică, G. Furtos, O. Lucaciu, P. Pascuta, M. Vlassa, M. Moldovan and R.-S. Campian, Electrospun Membranes Based on Polycaprolactone, Nano-Hydroxyapatite and Metronidazole, *Materials*, 2021, **14**, 931, DOI: 10.3390/ma14040931.

44 A. E. Tarabiah, H. A. Alhadlaq, Z. M. Alaizeri, A. A. A. Ahmed, G. M. Asnag and M. Ahamed, Enhanced Structural, Optical, Electrical Properties and Antibacterial Activity of PEO/CMC Doped ZnO Nanorods for Energy Storage and Food Packaging Applications, *J. Polym. Res.*, 2022, **29**, 167, DOI: 10.1007/s10965-022-03011-8.

45 A. Ghaee, S. Bagheri-Khoulenjani, H. Amir Afshar and H. Bogheiri, Biomimetic Nanocomposite Scaffolds Based on Surface Modified PCL-Nanofibers Containing Curcumin Embedded in Chitosan/Gelatin for Skin Regeneration, *Composites, Part B*, 2019, **177**, 107339, DOI: 10.1016/j.compositesb.2019.107339.

46 P. Mosallanezhad, H. Nazockdast, Z. Ahmadi and A. Rostami, Fabrication and Characterization of Polycaprolactone/Chitosan Nanofibers Containing Antibacterial Agents of Curcumin and ZnO Nanoparticles for Use as Wound Dressing, *Front. Bioeng. Biotechnol.*, 2022, **10**, 1027351, DOI: 10.3389/fbioe.2022.1027351.

47 M. Petriceanu, F. G. Ioniţă, R. R. Piticescu, A. I. Nicoară, A. C. Matei, M. A. Ioţa, I. A. Tudor, Ş. Caramarin and C. F. Ciobota, Effect of Doping ZrO2 on Structural and Thermal Properties, *Inorganics*, 2024, **12**, 290, DOI: 10.3390/inorganics12110290.

48 F. Shi, K. Liang and Z.-M. Qi, Investigation of the Crystal Structure, Lattice Vibration and Dielectric Property of SrZrO 3 Ceramic, *J. Mater. Res.*, 2016, **31**, 3249–3254, DOI: 10.1557/jmr.2016.340.

49 A. Talebi, S. Labbaf and F. Karimzadeh, A Conductive Film of Chitosan-Polycaprolcatone-Polypyrrole with Potential in Heart Patch Application, *Polym. Test.*, 2019, **75**, 254–261, DOI: 10.1016/j.polymertesting.2019.02.029.

50 M. Das, C. Dhand, G. Sumana, A. K. Srivastava, R. Nagarajan, L. Nain, M. Iwamoto, T. Manaka and B. D. Malhotra, Electrophoretic Fabrication of Chitosan-Zirconium-Oxide Nanobiocomposite Platform for Nucleic Acid Detection, *Biomacromolecules*, 2011, **12**, 540–547, DOI: 10.1021/bm1013074.

51 E. Sharifzadeh, M. Karami and F. Ader, Formation of Nanoparticle Aggregates and Agglomerates in Polymer Nanocomposites and Their Distinct Impacts on the Mechanical Properties, *Polym. Eng. Sci.*, 2023, **63**, 1303–1313, DOI: 10.1002/pen.26284.

52 X. Jiang, Y. Lin, X. Xuan, Y. Zhuo, J. Wu, J. He, X. Du, Z. Zhang and T. Li, Stiffening Surface Lowers Ice Adhesion Strength by Stress Concentration Sites, *Colloids Surf., A*, 2023, **666**, 131334, DOI: 10.1016/j.colsurfa.2023.131334.

53 M. Asmael, Z. A. Mahmoud, S. Sahmani and B. Safaei, Enhancing Tensile Strength, Adhesive Joining of CFPEEK and Microstructure Properties of Epoxy by Nd2O3 Rare-Earth Nanoparticles Reinforcement, *Mater. Today Commun.*, 2024, **41**, 110854, DOI: 10.1016/j.mtcomm.2024.110854.

54 S. Abdolmohammadi, S. Siyamak, N. A. Ibrahim, W. M. Z. W. Yunus, M. Z. A. Rahman, S. Azizi and A. Fatehi, Enhancement of Mechanical and Thermal Properties of Polycaprolactone/Chitosan Blend by Calcium Carbonate Nanoparticles, *Int. J. Mol. Sci.*, 2012, **13**, 4508–4522, DOI: 10.3390/ijms13044508.

55 S. Mafirad, M. R. Mehrnia, P. Zahedi and S. Hosseini, Chitosan-based Nanocomposite Membranes with Improved Properties: Effect of Cellulose Acetate Blending and TiO 2 Nanoparticles Incorporation, *Polym. Compos.*, 2018, **39**, 4452–4466, DOI: 10.1002/pc.24539.

56 C. Tan, C. Rudd, A. Parsons, N. Sharmin, J. Zhang, W. Chen and I. Ahmed, Chitosan as a Coupling Agent for Phosphate Glass Fibre/Polycaprolactone Composites, *Fibers*, 2018, **6**, 97, DOI: 10.3390/fib6040097.

57 J. M. Dennis, T. R. Long, A. Krishnamurthy, N. T. Tran, B. A. Patterson, C. E. Busch, K. A. Masser, J. L. Lenhart and D. B. Knorr, Influence of Hydroxyl Group Concentration on Mechanical Properties and Impact Resistance of ROMP Copolymers, *ACS Appl. Polym. Mater.*, 2020, **2**, 2414–2425, DOI: 10.1021/acsapm.0c00352.

58 L. Vladislavova, T. Smolorz, N. Orlovskaya, M. Lugovy, M. J. Reece, S. Köbel, A. Kopia, M. Makowska, T. Graule and G. Blugan, Strength Analysis and Stress-Strain Deformation Behavior of 3 Mol% Y-TZP and 21 Wt.% Al2O3-3 Mol% Y-TZP, *Materials*, 2021, **14**, 3903, DOI: 10.3390/ma14143903.

59 H. Zhang, L. Chen, X. Han, F. Jiang, H. Sun and D. Sun, Enhanced Mechanical Properties of Nylon6 Nanocomposites Containing Pristine α-Zirconium Phosphate Nanoplatelets of Various Sizes by Melt-Compounding, *RSC Adv.*, 2017, **7**, 32682–32691, DOI: 10.1039/C7RA05458K.

60 K. Chęcińska, M. Chęciński, M. Sikora, Z. Nowak, S. Karwan and D. Chlubek, The Effect of Zirconium Dioxide (ZrO2) Nanoparticles Addition on the Mechanical Parameters of Polymethyl Methacrylate (PMMA): A Systematic Review and Meta-Analysis of Experimental Studies, *Polymers*, 2022, **14**, 1047, DOI: 10.3390/polym14051047.

61 J. Wang, L. Gong, S. Xi, C. Li, Y. Su and L. Yang, Synergistic Effect of Interface and Agglomeration on Young's Modulus of Graphene-Polymer Nanocomposites, *Int. J. Solids Struct.*, 2024, **292**, 112716, DOI: 10.1016/j.ijsolstr.2024.112716.

62 T. Bhatnagar, P. Baxi, K. Sharma, G. Nijhawan, S. Jugran, K. Satyanarayana, L. Sharma and M. Alhadrawi, Unlocking the Strength of Nanocomposites: Mitigating the Impact of Nanoparticle Agglomeration on Tensile Performance, *E3S Web Conf.*, 2024, **588**, 01007, DOI: 10.1051/e3sconf/202458801007.

63 P. Wei, Z. Chen, S. Yao, X. Huang, B. Li, Y. Chen, Z. Huang and B. Lu, Enhancing Strength and Ductility of Graphene and ZrO2 Nanoparticles Hybrid Reinforced AA2024 Composite Fabricate by Laser Powder Bed Fusion, *Composites, Part A*, 2024, **185**, 108378, DOI: 10.1016/j.compositesa.2024.108378.

64 M. Pandey, G. M. Joshi, K. Deshmukh and J. Ahmad, Impedance Spectroscopy And Conductivity Studies Of CdCl2 Doped Polymer Electrolyte, *Adv. Mater. Lett.*, 2015, **6**, 165–171, DOI: 10.5185/amlett.2015.5639.

65 S. P. Ansari and F. Mohammad, Electrical Studies on the Composite of Polyaniline with Zinc Oxide Nanoparticles, *IUP J. Chem.*, 2010, **4**, 7–18.

66 R. Divya, M. Meena, C. K. Mahadevan and C. M. Padma, Formation and Properties of ZnO Nanoparticle Dispersed PVA Films, *Int. J. Eng. Res. Technol.*, 2014, **3**, 722–727.

67 P. L. Reddy, K. Deshmukh, K. Chidambaram, M. M. N. Ali, K. K. Sadasivuni, Y. R. Kumar, R. Lakshmipathy and S. K. K. Pasha, Dielectric Properties of Polyvinyl Alcohol (PVA) Nanocomposites Filled with Green Synthesized Zinc Sulphide (ZnS) Nanoparticles, *J. Mater. Sci.: Mater. Electron.*, 2019, **30**, 4676–4687, DOI: 10.1007/s10854-019-00761-y.

68 F. H. Alshammari, Fabrication and Characterization of Novel PCL/TiO2/Cr2O3 Nanocomposites for Advanced Dielectric Applications, *J. Mater. Sci.: Mater. Electron.*, 2025, **36**, 416, DOI: 10.1007/s10854-025-14481-z.

69 A. M. Alshehri, D. Domyati, M. A. El-Morsy, M. O. Farea and A. A. Menazea, Dielectric Properties and Optical Characteristics of PVA-Chitosan Blend Incorporated by Al2O3 and V2O5 Nanoparticles Prepared via Lased Ablation and Their Potential for Electrical Applications, *J. Mater. Sci.: Mater. Electron.*, 2025, **36**, 654, DOI: 10.1007/s10854-025-14694-2.

70 X. Zhang, Y. Zhang, X. Zhang and S. Guo, Interface Design and Dielectric Response Behavior of SiO2/PB Composites with Low Dielectric Constant and Ultra-Low Dielectric

Loss, *Surf. Interfaces*, 2021, **22**, 100807, DOI: 10.1016/j.surfin.2020.100807.

71 C. Li, G. Chen, X. Qiu, Q. Lou and X. Gao, A Direct Proof for Maxwell–Wagner Effect of Heterogeneous Interface, *AIP Adv.*, 2021, **11**, 065227, DOI: 10.1063/5.0040947.

72 F. Fernández-Gil, F. Olate-Moya, J. R. Aguilar-Cosme, J. García-Molleja, J. P. Fernández-Blázquez, S. Cartmell and H. Palza, Micro-Arranged ZnO Particles and Conductive Fillers in PCL Composites for Enhanced Piezoelectric and Dielectric Properties in Bone Tissue Engineering Applications, *Mater. Des.*, 2025, **251**, 113672, DOI: 10.1016/j.matdes.2025.113672.

73 A. Rajeh, H. M. Ragab and M. M. Abutalib, Co Doped ZnO Reinforced PEMA/PMMA Composite: Structural, Thermal, Dielectric and Electrical Properties for Electrochemical Applications, *J. Mol. Struct.*, 2020, **1217**, 128447, DOI: 10.1016/j.molstruc.2020.128447.

74 M. O. Aydogdu, N. Ekren, M. Suleymanoglu, S. Erdem-Kuruca, C.-C. Lin, E. Bulbul, M. N. Erdol, F. N. Oktar, U. K. Terzi, O. Kilic, *et al.*, Novel Electrospun Polycaprolactone/Graphene Oxide/Fe3O4 Nanocomposites for Biomedical Applications, *Colloids Surf., B*, 2018, **172**, 718–727, DOI: 10.1016/j.colsurfb.2018.09.035.

75 S. Mallakpour and N. Nouruzi, Modification of Morphological, Mechanical, Optical and Thermal Properties in Polycaprolactone-Based Nanocomposites by the Incorporation of Diacid-Modified ZnO Nanoparticles, *J. Mater. Sci.*, 2016, **51**, 6400–6410, DOI: 10.1007/s10853-016-9936-1.

76 A. Omar, R. Badry, M. A. Hegazy, I. S. Yahia, H. Elhaes, H. Y. Zahran, M. A. Ibrahim and A. Refaat, Enhancing the Optical Properties of Chitosan, Carboxymethyl Cellulose, Sodium Alginate Modified with Nano Metal Oxide and Graphene Oxide, *Opt. Quantum Electron.*, 2022, **54**, 806, DOI: 10.1007/s11082-022-04107-7.

77 A. P. Indolia and M. S. Gaur, Optical Properties of Solution Grown PVDF-ZnO Nanocomposite Thin Films, *J. Polym. Res.*, 2013, **20**, 43, DOI: 10.1007/s10965-012-0043-y.

78 H. M. Shanshool, M. Yahaya, W. M. M. Yunus and I. Y. Abdullah, Measurements of Nonlinear Optical Properties of PVDF/ZnO Using Z-Scan Technique, *Braz. J. Phys.*, 2015, **45**, 538–544, DOI: 10.1007/s13538-015-0345-8.

79 F. Gharbi, K. Benthami, T. H. Alsheddi, M. M. E. Barakat, N. Alnaim, A. Alshoaibi and S. A. Nouh, Structural, Thermal, and Optical Studies of Gamma Irradiated Polyvinyl Alcohol-, Lignosulfonate-, and Palladium Nanocomposite Film, *Polymers*, 2022, **14**(13), 2613, DOI: 10.3390/polym14132613.

80 A. J. Kadham, D. Hassan, N. Mohammad and A. Hashim, Fabrication of (Polymer Blend-Magnesium Oxide) Nanoparticle and Studying Their Optical Properties for Optoelectronic Applications, *Bull. Electr. Eng. Informatic.*, 2018, **7**, 28–34, DOI: 10.11591/eei.v7i1.839.

81 E. Kubyshkina and M. Unge, Impact of Interfacial Structure on the Charge Dynamics in Nanocomposite Dielectrics, *J. Appl. Phys.*, 2019, **125**, 045109, DOI: 10.1063/1.5078800.

82 M. S. Sikder, M. R. Rahman, M. Al-Mamun, M. S. S. Chowdhury and M. M. Haque, Structural and Mechanical Properties of Chitosan Doped with Zirconium Oxide, *Int. J. Adv. Sci. Res. Eng.*, 2020, **06**, 55–60, DOI: 10.31695/IJASRE.2020.33852.

83 P. Mosallanezhad, H. Nazockdast, Z. Ahmadi and A. Rostami, Fabrication and Characterization of Polycaprolactone/Chitosan Nanofibers Containing Antibacterial Agents of Curcumin and ZnO Nanoparticles for Use as Wound Dressing, *Front. Bioeng. Biotechnol.*, 2022, **10**, 1027351, DOI: 10.3389/fbioe.2022.1027351.

84 Z.-Y. Liu, X. Cai, C.-X. Zhang, R.-Y. Cao, Y.-Y. Liu and H.-X. Deng, Oxygen Vacancy Related Hole Fast Trapping in High Mobility Cubic-Ge/ZrO 2 Interface, *J. Phys. D Appl. Phys.*, 2023, **56**, 105101, DOI: 10.1088/1361-6463/acbaa8.

85 S. Song, J. Wei, X. He, G. Yan, M. Jiao, W. Zeng, F. Dai and M. Shi, Oxygen Vacancies Generated by Sn-Doped ZrO 2 Promoting the Synthesis of Dimethyl Carbonate from Methanol and CO 2, *RSC Adv.*, 2021, **11**, 35361–35374, DOI: 10.1039/D1RA07060F.

86 A. S. Berestennikov, Y. Li, I. V. Iorsh, A. A. Zakhidov, A. L. Rogach and S. V. Makarov, Beyond Quantum Confinement: Excitonic Nonlocality in Halide Perovskite Nanoparticles with Mie Resonances, *Nanoscale*, 2019, **11**, 6747–6754, DOI: 10.1039/C8NR09837A.

87 E. F. d. Reis, F. S. Campos, A. P. Lage, R. C. Leite, L. G. Heneine, W. L. Vasconcelos, Z. I. P. Lobato and H. S. Mansur, Synthesis and Characterization of Poly (Vinyl Alcohol) Hydrogels and Hybrids for RMPB70 Protein Adsorption, *Mater. Res.*, 2006, **9**, 185–191, DOI: 10.1590/S1516-14392006000200014.

88 A. Alsaad, A. R. Al Dairy, A. Ahmad, I. A. Qattan, S. Al Fawares and Q. Al-Bataineh, Synthesis and Characterization of Polymeric (PMMA-PVA) Hybrid Thin Films Doped with TiO2 Nanoparticles Using Dip-Coating Technique, *Crystals*, 2021, **11**, 99, DOI: 10.3390/cryst11020099.

89 V. S. Sangawar and M. C. Golchha, Evolution of the Optical Properties of Polystyrene Thin Films Filled with Zinc Oxide Nanoparticles, *Int. J. Sci. Eng. Res.*, 2013, **4**, 2700–2705.

90 M. K. Mohammed, T. N. Khudhair, K. S. Sharba, A. Hashim, Q. M. Hadi and M. H. Meteab, Tuning the Morphological and Optical Characteristics of SnO2/ZrO2 Nanomaterials Doped PEO for Promising Optoelectronics Applications, *Rev. Compos. Mater. Av.*, 2024, **34**, 495–503, DOI: 10.18280/rcma.340411.

91 C.-L. Tsai and G.-S. Liou, Highly Transparent and Flexible Polyimide/ZrO 2 Nanocomposite Optical Films with a Tunable Refractive Index and Abbe Number, *Chem. Commun.*, 2015, **51**, 13523–13526, DOI: 10.1039/C5CC05301C.

92 J. Gu, X. Wang, C. Xu, X. Feng and S. Zhang, Polythiourethane Composite Film with High Transparency, High Refractive Index and Low Dispersion Containing ZnS Nanoparticle via Thiol-Ene Click Chemistry, *Macromol. Res.*, 2023, **31**, 603–613, DOI: 10.1007/s13233-023-00144-7.

93 P. Nivetha, R. Siranjeevi, R. Susmitha, S. S. Shabnum, C. K. Raj, K. Benazir, A. Saravanan and A. S. Vickram, A Comprehensive Review on Advances in Synthesis and Characterization of Nanocomposite: Current Status and Emerging Applications, *Environ. Qual. Manag.*, 2025, **35**(1), e70108, DOI: **10.1002/tqem.70108**.

94 Z. S. Jaber, M. A. Habeeb and W. H. Radi, Synthesis and Characterization of (PVA-CoO-ZrO2) Nanostructures for Nanooptoelectronic Fields, *East Eur. J. Phys.*, 2023, 228–233, DOI: **10.26565/2312-4334-2023-2-25**.

95 A. R. Ali Emad Nief, Abdulridha Improvement of the Structural and Electrical Properties of PVA through the Addition of $Bi_2O_3$ and $SiO_2$ Nanoparticles for Electronic Devices, *Int. J. Comput. Exp. Sci. Eng.*, 2025, **11**(1), 1344–1349, DOI: **10.22399/ijcesen.1042**.

96 C. R. Arciola, D. Campoccia and L. Montanaro, Implant Infections: Adhesion, Biofilm Formation and Immune Evasion, *Nat. Rev. Microbiol.*, 2018, **16**, 397–409, DOI: **10.1038/s41579-018-0019-y**.

97 J. Venkatesan, J.-Y. Lee, D. S. Kang, S. Anil, S.-K. Kim, M. S. Shim and D. G. Kim, Antimicrobial and Anticancer Activities of Porous Chitosan-Alginate Biosynthesized Silver Nanoparticles, *Int. J. Biol. Macromol.*, 2017, **98**, 515–525, DOI: **10.1016/j.ijbiomac.2017.01.120**.

98 E. Ghasemian Lemraski, H. Jahangirian, M. Dashti, E. Khajehali, M. S. Sharafinia, R. Rafiee-Moghaddam and T. J. Webster, Antimicrobial Double-Layer Wound Dressing Based on Chitosan/Polyvinyl Alcohol/Copper: In Vitro and in Vivo Assessment, *Int. J. Nanomed.*, 2021, **16**, 223–235, DOI: **10.2147/IJN.S266692**.

99 A. Saeed, I. Guizani, F. E. Hanash, G. M. Asnag, A. M. Al-Harthi, R. Alwafi, T. F. Qahtan, M. A. Morsi and A. S. Assran, Enhancing Optical, Structural, Thermal, Electrical Properties, and Antibacterial Activity in Chitosan/Polyvinyl Alcohol Blend with ZnO Nanorods: Polymer Nanocomposites for Optoelectronics and Food/Medical Packaging Applications, *Polym. Bull.*, 2024, **81**, 11645–11670, DOI: **10.1007/s00289-024-05270-5**.

100 N. Tabassum, D. Kumar, D. Verma, R. A. Bohara and M. P. Singh, Zirconium Oxide (ZrO2) Nanoparticles from Antibacterial Activity to Cytotoxicity: A next-Generation of Multifunctional Nanoparticles, *Mater. Today Commun.*, 2021, **26**, 102156, DOI: **10.1016/j.mtcomm.2021.102156**.

101 R. Al-Wafi, S. F. Mansour, M. S. AlHammad and M. K. Ahmed, Biological Response, Antibacterial Properties of ZrO2/Hydroxyapatite/Graphene Oxide Encapsulated into Nanofibrous Scaffolds of Polylactic Acid for Wound Healing Applications, *Int. J. Pharm.*, 2021, **601**, 120517, DOI: **10.1016/j.ijpharm.2021.120517**.

102 Z. Breijyeh, B. Jubeh and R. Karaman, Resistance of Gram-Negative Bacteria to Current Antibacterial Agents and Approaches to Resolve It, *Molecules*, 2020, **25**, 1340, DOI: **10.3390/molecules25061340**.

103 E. O. Mikhailova, Green Silver Nanoparticles: An Antibacterial Mechanism, *Antibiotics*, 2024, **14**, 5, DOI: **10.3390/antibiotics14010005**.